ACS APPLIED ENERGY MATERIALS

www.acsaem.org Article

Modulation of Surface Structure and Electronic States of Defective Pd-Doped NiFe-Layered Double Hydroxide Bifunctional Electrocatalyst by Alkaline Etching for Zn−Air Batteries

Beibei Wang,[⊥] Youyuan Zhang,[⊥] Dajun Wu, Fanya Jin, Zhenzhong Yang,* Shaohui Xu,* Dayuan Xiong, Lianwei Wang, and Paul K. Chu

Cite This: *ACS Appl. Energy Mater.* 2025, 8, 12857−12867 Read Online

ACCESS | Metrics & More | Article Recommendations | Supporting Information

ABSTRACT: Surface structure and electronic states are important parameters for bifunctional catalysts, especially in energy devices. Herein, the hierarchically porous defective Pd-doped NiFe-layered double hydroxide is prepared by electrodeposition and alkaline etching. The etching process increases the surface area to facilitate bifunctional catalysis of the oxygen reduction reaction/oxygen evolution reaction in Zn−air batteries (ZABs). Electrochemical assessment reveals inhibited oxidation of nickel hydroxide after alkaline etching and formation of the hybrid battery composed of Zn−Ni and ZABs, which shows high reversibility and stability. The results reveal an effective strategy to modulate the surface properties of bifunctional catalysts.

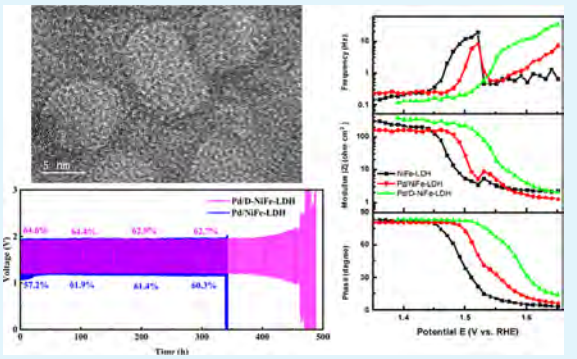

KEYWORDS: *Pd doping, defective NiFe-layered double hydroxide, hierarchical porous structure, bifunctional electrocatalyst, Zn−air battery*

1. INTRODUCTION

In the development of electrochemical energy storage and conversion devices, high-efficiency and activity bifunctional electrocatalysts are desired.[1−3] Catalysts for the oxygen reduction reaction (ORR) and oxygen evolution reaction (OER) in metal-air batteries such as aqueous Zn−air batteries (ZABs) must have a high energy density, low production cost, high safety, and environmental friendliness.[2] In particular, low overpotentials in OER and ORR are crucial in order to reduce the charging voltage and increase the discharge voltage of ZABs.[2,4−6] Pt and Pd nanoparticles and/or single atom catalysts exhibit good activity in ORR, while NiFe-layered double hydroxides (NiFe-LDHs) deliver excellent OER performance.[4,6,7] However, the OER and ORR suffer from slow kinetics and large overpotentials, consequently limiting the energy density and cycling life of ZABs. Therefore, it is important to identify better bifunctional catalysts for ZABs.[7,8]

Hierarchical porous electrodes show enhanced electrocatalytic activity in energy devices, such as supercapacitors and metal-air batteries.[9−11] The hierarchical porous structure provides abundant contact with the electrolyte, shortens the ion diffusion paths during electrochemical processes, and improves the kinetics and long-term stability. Supercapacitors fabricated by three-dimensional (3D) hierarchical porous materials combining microporous cores, mesoporous walls, and micropores have high energy and power densities at high rates due to the small resistance, ion-buffering reservoir, and short diffusion distance. The mesoporous walls provide low-resistance pathways for ions through the pores, while the micropores strengthen the electric-double-layer capacitance.[9] The hierarchical porous structure has been adopted for dual-atom FeNi−N_8−C to provide high-efficiency ORR catalysis. The aqueous ZAB shows a maximum power density of 367.1 mW cm^{-2} in addition to good stability.[10] The rechargeable aqueous zinc-ion batteries comprising the Zn anode and hierarchically porous vanadium oxide cathode show a high specific capacity of 426 mA·h g^{-1} at 0.2 A g^{-1} as well as long-term cyclic stability with a capacity retention of 96% for 20,000 cycles at 10 A g^{-1}.[11]

Dealloying is a simple and effective approach to produce mesopores and/or micropores on the porous electrode surface.[12−16] During the dealloying process, the less stable metal component is etched selectively from the conductive porous alloy electrode to create defective states in conjunction with nanopores and walls. In the hierarchical porous structure,

Received: July 4, 2025
Revised: August 17, 2025
Accepted: August 20, 2025
Published: August 27, 2025

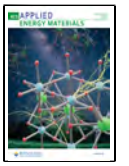

https://doi.org/10.1021/acsaem.5c02043
ACS Appl. Energy Mater. 2025, 8, 12857−12867

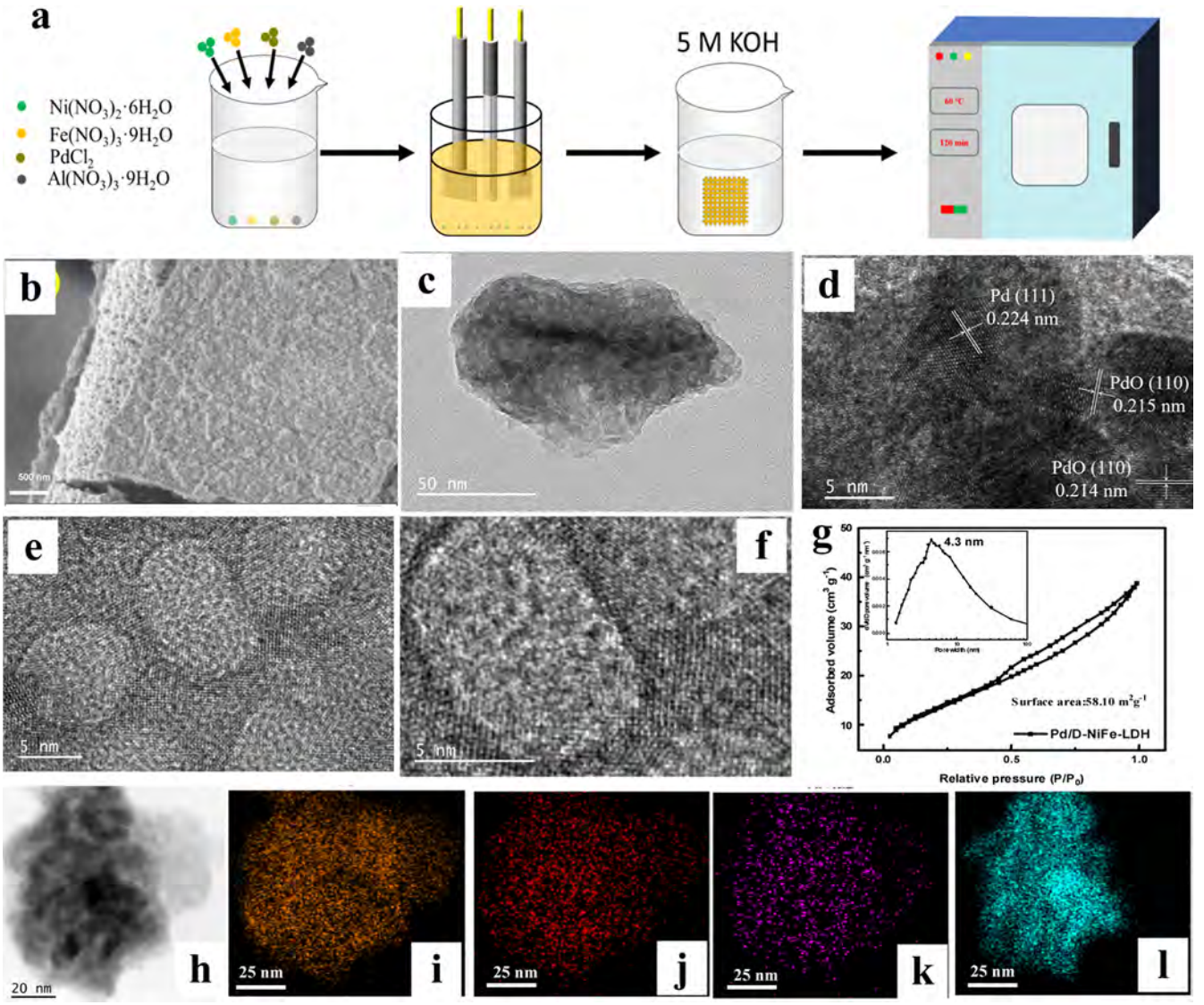

Figure 1. Microstructure characterization of Pd-doped NiFe-LDH. (a) Schematic illustration of synthesis route to Pd/D-NiFe-LDH. (b) SEM and (c-f) TEM images of Pd/D-NiFe-LDH. (g) N_2 adsorption−desorption isotherms and pore size distribution (inset). (h)TEM image and EDS elemental mapping of (i) Fe, (j) Ni, (k) Al, and (l) Pd element.

the microporous (>10 μm) substrate has a 3D structure with a large surface area and a nanometer-scale mesoporous structure (10−100 nm). Different electrochemical processes can be used to enhance the electrocatalytic process, including the introduction of ions in the microporous cores, transporting ions through the mesoporous walls, and confining ions in the micropores.[9] Dealloying also changes the electronic state. By performing etching of Mo in an alkaline solution, the NiFeMoO precatalyst is converted into the OER-active NiFeOOH/NiFe-LDH with optimum OER activity.[12,13] The gradual dissolution of Mo during the OER forms a porous structure to improve electrolyte transfer. Higher OER activity has been observed after introducing Al into ultrathin trinary Ni_3FeAl_x-LDH on Ni foam. After the partial dissolution of Al^{3+} species on the catalyst surface to form the hierarchical porous structure, low-coordination Ni and Fe, as well as defects, are formed to improve the OER activity.[14] Formation of single-atomic-site ruthenium on defective nickel−iron LDH nanosheets after Al etching in an alkaline solution gives rise to superior HER and OER properties in the alkaline medium, including a low overpotential, high current density, and long-term durability.[17] In this work, a hierarchical porous structure is formed on defective Pd-doped NiFe-LDH by alkaline etching. The optimal surface morphology and electronic states improve the catalytic properties in both the OER and ORR. The ORR/OER bifunctional electrocatalyst is assembled into rechargeable ZABs to demonstrate the high application potential.

2. RESULTS AND DISCUSSION

2.1. Structure. The defective Pd-doped NiFe-LDH (denoted as Pd/D-NiFe-LDH) is fabricated on a piece of carbon cloth (CC) by electrodeposition and subsequent etching, as shown in Supporting Information (Experimental details). The electrodeposited Pd/NiFe-LDH and Pd/D-NiFe-LDH samples are amorphous and do not show XRD peaks (Figure S1a). The NiFe-LDH structure is confirmed by the Raman scattering spectra (Figure S1b), which show peaks at 527 and 692 cm^{-1} corresponding to the Ni−O and FeOOH, respectively.[18] Our experiments reveal that 1.4 mmol L^{-1} (25

https://doi.org/10.1021/acsaem.5c02043
ACS Appl. Energy Mater. 2025, 8, 12857−12867

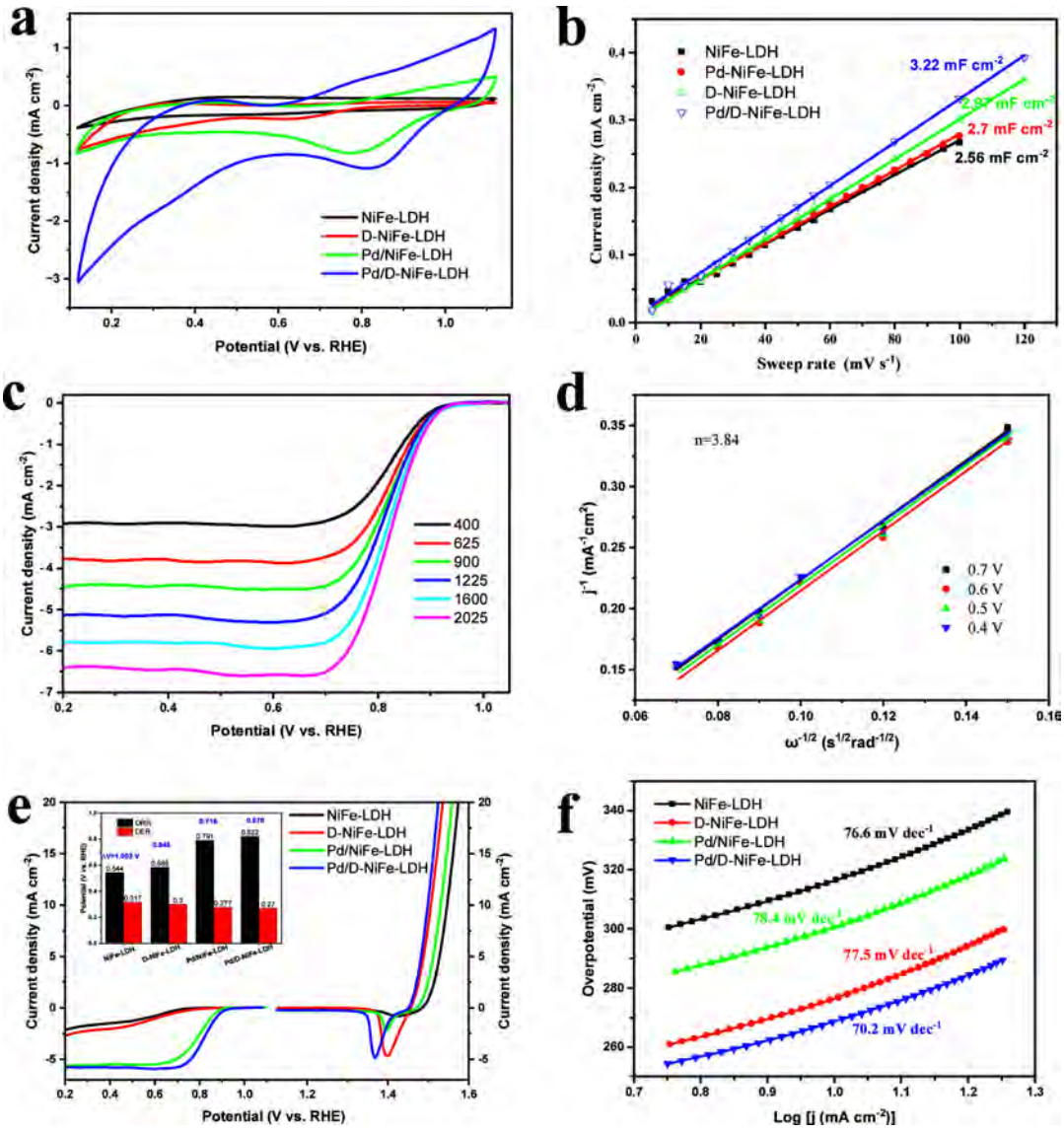

Figure 2. Catalytic properties of Pd/D-NiFe-LDH. (a) Cyclic voltammogram (CV) curves in oxygen atmosphere, sweep rate 100 mV s^{-1}. (b) Relationship of current density versus sweeping rate to obtain the double layer capacitance. (c) Linear sweep voltammetry (LSV) curves obtained at various rotation rates for Pd/D-NiFe-LDH (sweeping rate 10 mV s^{-1}) and the related (d) Koutecky−Levich plots. (e) Overall polarization curves of ORR and OER bifunctional curves, and related potential value shown inset and (f) Tafel plots of OER process.

mg) $PdCl_2$ and 24 h etching are optimal, corresponding to the high performance of ORR and OER, as shown in Figures S2 and S3.

The surface morphology of Pd/D-NiFe-LDH is characterized by scanning electron microscopy (SEM), as shown in Figure 1b. The porous structure is composed of uniformly distributed nanoparticles on CC. The nanoparticles have a diameter of about 50 nm (Figure 1c). The high-resolution TEM image of Pd/D-NiFe-LDH (Figure 1d) shows a stripe pattern, and the spacing between stripes is about 0.224 nm, corresponding to the Pd (111) plane, and the spacing of 0.215 nm corresponds to the (110) plane of Pd oxide.[19,20] The Pd and PdO particles are 5−10 nm. A mesoporous structure is formed on the surface with a diameter of 5 nm (Figure 1e), resulting from KOH etching of Al. After etching, a mesoporous well (∼5 nm) and a microporous structure (∼1 nm) are formed, as shown in Figure 1f. Fe, Ni, Al, and Pd elements are observed from Pd/D-NiFe-LDH by EDS, and their distributions are uniform (Figure 1h−l). The nitrogen isotherm of the Pd/D-NiFe-LDH shows the combined characteristics of types I and II (Figure 1g),[9] with a Brunauer−Emmett−Teller (BET) surface area of 58.10 m^2 g^{-1} and an average pore diameter of 4.3 nm, which are consistent with TEM. The results indicate that the 3D hierarchical porous structure is formed for defective Pd-doped NiFe-LDH, which contains microporous structures as ion-buffering reservoirs, mesoporous walls with small ion-transfer resistance, and micropores for charge accommodation.

XPS spectra are acquired to analyze the surface electronic state after etching (Figure S4). The XPS spectrum of Ni does not change after the KOH etching. The XPS spectrum of Fe shows a 0.3 eV negative shift and a 0.2 eV positive shift for Pd 3d after etching. The etching process changes the electronic state of different elements and decreases electron concentration around Pd, and the Pd^{2+} electronic state would be attributed to the PdO phase observed in the TEM study, which would be contributed to the adsorption of O_2 and better splitting of the O−O bond.[19,20] The percentage of oxidation-

https://doi.org/10.1021/acsaem.5c02043
ACS Appl. Energy Mater. 2025, 8, 12857−12867

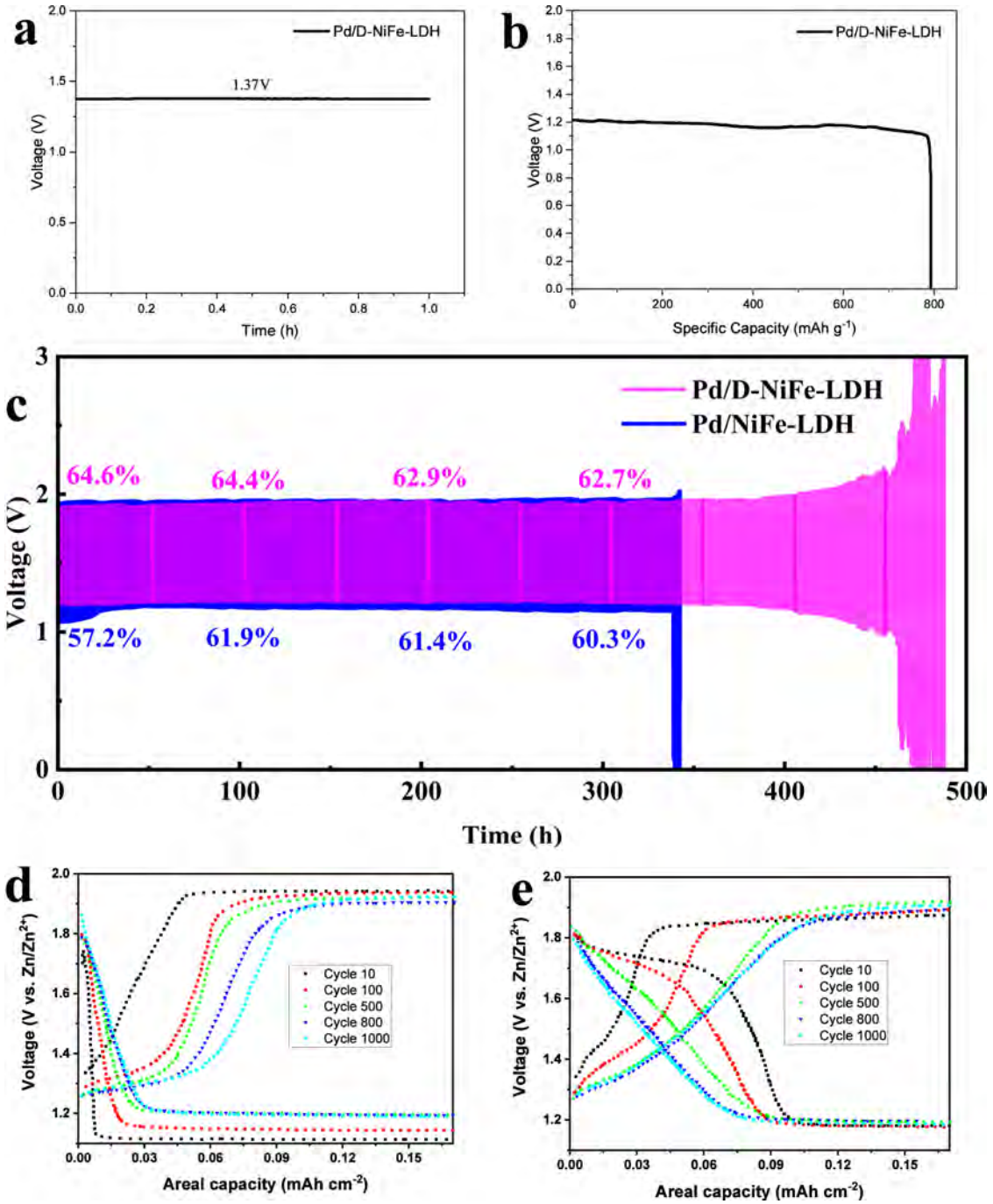

Figure 3. Performances of Zn−air battery with Pd/D-NiFe-LDH as cathode catalysts. (a) Open circuit voltage during 1 h. (b) Discharge performance of Zn−air battery (current density 1 mA cm^{-2}). (c) Charge−discharge profiles (current density 2 mA cm^{-2}). Galvanostatic voltage profiles of ZABs at different cycle numbers for (d) Pd/NiFe-LDH and (e) Pd/D-NiFe-LDH.

defective states increases from 56.5% (Pd/NiFe-LDH) to 67.6% (Pd/D-NiFe-LDH), as shown in the O 1s spectra. The introduced defective states are expected to enhance the catalytic activity.[21,22]

2.2. Electrocatalytic Activity and ZABs. In order to evaluate the bifunctional electrocatalytic properties of Pd/D-NiFe-LDH, the electrochemical properties are investigated in a three-electrode cell containing a 1.0 mol-L^{-1} KOH solution. The cyclic voltammogram (CV) curves of Pd/D-NiFe-LDH are obtained in the oxygen and nitrogen atmospheres (Figure S5). It shows that the high electrochemical reaction in an oxygen atmosphere corresponds to large current densities in the potential region between 0.1 and 1.0 V vs RHE, especially the reduction peak at a potential of 0.85 V vs RHE. The CV curves of different electrodes in oxygen are shown in Figure 2a. After the Pd-doping process, the additional reduction peak at potential 0.85 V vs RHE would be attributed to the reaction process of Pd.[23−25] After KOH etching (Pd/D-NiFe-LDH), the potential of the reduction peak shifts from 0.79 to 0.82 V vs RHE, and the current density increases from 0.82 to 1.1 mA cm^{-2}.

KOH etching affects the surface morphology and increases the surface area. The double layer capacitance C_{dl} is derived from the CVs in the open-circuit potential (OCP) region at

https://doi.org/10.1021/acsaem.5c02043
ACS Appl. Energy Mater. 2025, 8, 12857−12867

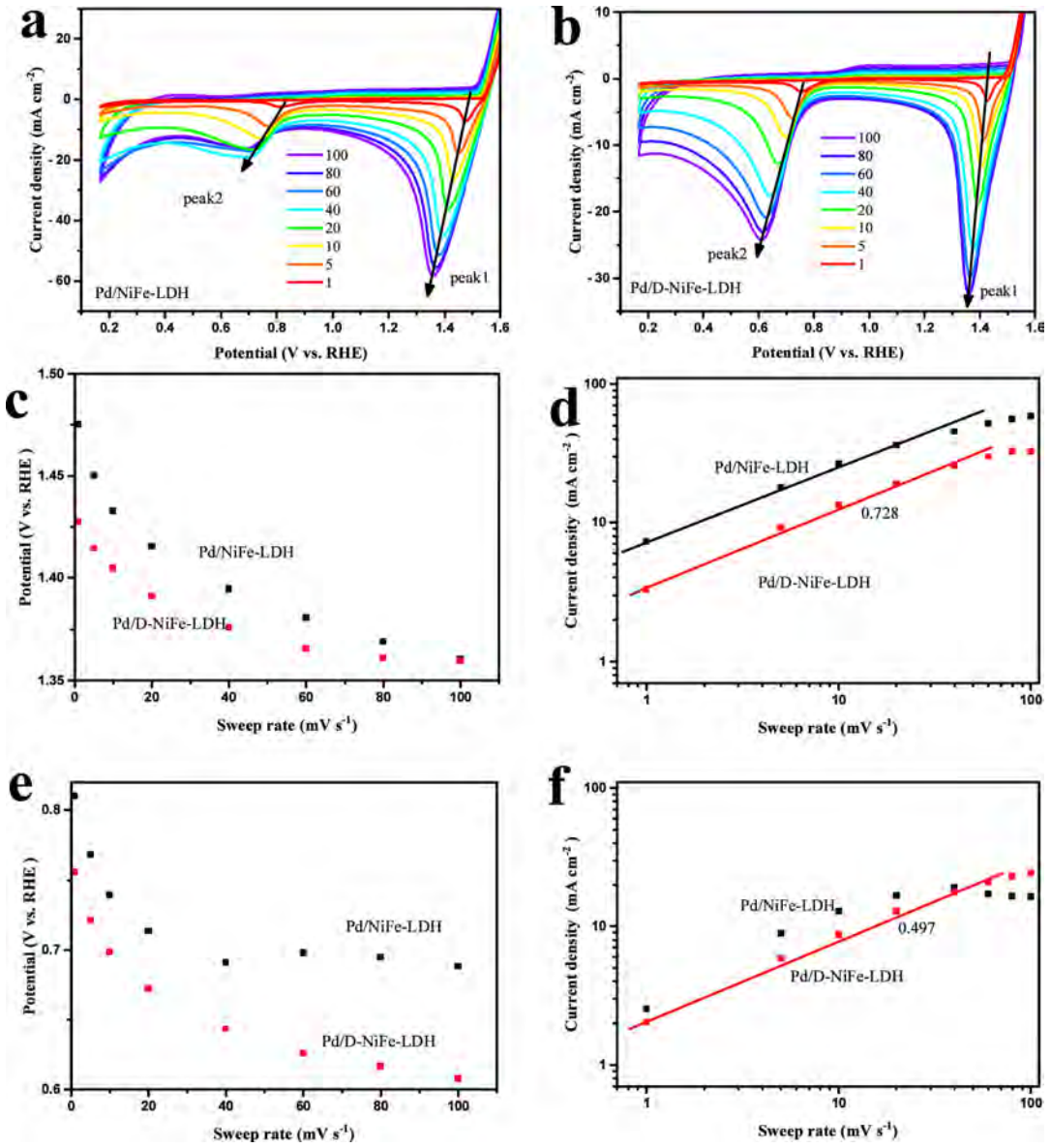

Figure 4. Electrochemical characterization of catalysts. Cyclic voltammogram (CV) curves at different sweep rates for (a) Pd/NiFe-LDH and (b) Pd/D-NiFe-LDH, and (c, e) potentials and (d, f) current densities versus sweeping rates for the cathodic peaks at potential region 1.4 (c, d) and 0.7 (e, f) V vs RHE, respectively.

scanning rates between 5 and 100 mV s^{-1} (Figure S6). After the Pd-doping process, the double layer capacitance increases from 2.56 (NiFe-LDH) to 2.7 (Pd−NiFe-LDH) mF cm^{-2}. After KOH etching, the double layer capacitance increases to 3.22 mF cm^{-2} for Pd/D-NiFe-LDH. Even, the KOH etching process would also increase the double layer capacitance to 2.97 mF cm^{-2} for NiFe-LDH. The increasing surface area after etching would be attributed to the formation of surface mesoporous and microporous structures.

To elucidate the electrocatalytic mechanism, the ORR properties are studied on a rotating disk electrode in 0.1 mol L^{-1} KOH after attaching the sample with Nafion to a glass carbon electrode. The ORR polarization curves are recorded at different rotational speeds (Figure 2c). LSV shows increasing current densities from 3 to 6.5 mA cm^{-2} as the rotation rate goes up from 400 to 2025 rpm (RPM) for Pd/D-NiFe-LDH (potential region from 0.2 to 1.1 V vs RHE). The corresponding Koutecky−Levich (K-L) plots for different potentials are shown in Figure 2d. The linear relationship between the current density and scanning speeds indicates first-order reaction kinetics for dissolved oxygen.[26,27] Based on the linear slope, the electron transfer number (n) during the ORR is obtained. The four-electron reaction is the main process, and the maximum electron transfer number n = 3.84 is obtained for Pd/D-NiFe-LDH, which is larger than that of Pd/NiFe-LDH (n = 3.69, Figure S7).

In order to show the bifunctionalities, the LSV curves for the ORR and the OER are shown in Figure 2e. The excellent oxygen reduction process of Pd/D-NiFe-LDH is identified from the ORR curves, as manifested by a large current density of 6 mA cm^{-2} at 0.6 V, which is larger than those of Pd/NiFe-LDH (5.55 mA cm^{-2}), D-NiFe-LDH, and NiFe-LDH (less than 2.0 mA cm^{-2}). Pd/D-NiFe-LDH exhibits the highest half-wave potential ($E_{1/2}$) of 822 mV that is positive compared to those of Pd/NiFe-LDH (791 mV), D-NiFe-LDH (585 mV), and NiFe-LDH (544 mV) (Figure 2e inset). After KOH

https://doi.org/10.1021/acsaem.5c02043
ACS Appl. Energy Mater. 2025, 8, 12857−12867

etching, the overpotential of the OER also decreases (Figure 2e and inset). The overpotential decreases from 0.277 V (Pd/NiFe-LDH) to 0.27 V for Pd/D-NiFe-LDH. The overpotential also decreases from 0.317 V (NiFe-LDH) to 0.3 V for D-NiFe-LDH after KOH etching. The Tafel slopes obtained by LSV are analyzed to study the OER mechanisms and limiting steps. A small Tafel slope is observed from Pd/D-NiFe-LDH (70.2 mV dec^{-1}) compared to Pd/D-NiFe-LDH (78.4 mV dec^{-1}) (Figure 2f). The Tafel slopes show that the rate-determining step (RDS) in OER is the third step of OH^- adsorption[28] for Pd/D-NiFe-LDH. The bifunctional catalytic activity is assessed by the overall oxygen electrode activity defined as the potential difference between OER and ORR, $\Delta E = E_1 - E_{1/2}$, where E_1 represents the potential required to generate a current density of 10 mA cm^{-2} in OER and $E_{1/2}$ is the half-wave potential in ORR.[29] As shown by the ORR and OER data (Figure 2e inset), Pd/D-NiFe-LDH has the smallest potential difference in ΔE (0.678 V) compared to Pd/NiFe-LDH (0.716 V), D-NiFe-LDH (0.945 V), and NiFe-LDH (1.003 V).

To further investigate the bifunctional catalytic properties, ZABs are fabricated with Pd/D-NiFe-LDH catalyst-coated carbon paper as a cathode, a zinc foil as the anode, and an alkaline electrolyte (6 mol L^{-1} KOH + 0.2 mol L^{-1} $Zn(AC)_2$) (Experimental details). The stability voltage (1.37 V) is maintained during the 1 h under the open-circuit condition (Figure 3a). The full discharge capacity is 793 mAh g^{-1} at a current density of 1 mA cm^{-2} (Figure 3b). The ZAB consisting of the Pd/D-NiFe-LDH positive electrode shows a peak power density of 114.7 mW cm^{-2} at the current density 250 mA cm^{-2}. The open voltage is 2.78 V for the two ZABs in series (Figure S8).

The stability of the ZABs made of the Pd/D-NiFe-LDH cathode is evaluated. It can operate for more than 450 h at a current density 2 mA cm^{-2} (Figure 3c), which is longer than ZABs consisting of the Pd/NiFe-LDH cathode (340 h). It also has high stability compared to that of other state-of-the-art ZABs (Table S1). Furthermore, Pd/D-NiFe-LDH-based ZAB shows excellent reversible energy efficiency. The initial energy efficiency is 64.6% (first 50 h) and decreases to 64.4%, 62.9%, and 62.7% every 100 h, reaching 59.6% in the last 100 h period, respectively. The reversible energy efficiency of the Pd/NiFe-LDH-based ZAB is 57.2% in the initial 50 h, increases to 61.9% in the next 100 h period, and decreases to 61.4% and 60.3% in the subsequent 100 h periods. The merits stem from the larger surface area and improved electronic properties after etching.

In order to understand the reaction process, the galvanostatic charging−discharging profiles of ZABs are shown in Figure 3d and Figure 3e for Pd/NiFe-LDH and Pd/D-NiFe-LDH, respectively. Compared to the voltage profiles of the Zn−air battery composed of a NiFe-LDH cathode (Figure S9), the Pd/NiFe-LDH-based Zn−air battery shows decreasing charging voltage (from 2.2 to 1.9 V) and increasing discharge voltage (from 1.0 to 1.1 V) due to the improved OER and ORR performance after Pd doping. After KOH etching, Pd/D-NiFe-LDH-based ZAB shows two discharge processes at 1.75 and 1.2 V, corresponding to Ni−Zn and ZABs, respectively.[30] The two discharging processes would also be identified from the galvanostatic charging/discharging profiles at 100th to 103rd cycles (Figure S10). The discharge voltage of the Ni−Zn battery disappears after 500 cycles (Figure 3e). The improved stability of the Pd/D-NiFe-LDH-based Zn−air battery would be attributed to reduction processes of NiFe-LDH after etching.[31]

2.3. Electrochemical Characteristics. The redox processes of Pd/D-NiFe-LDH after Pd doping and KOH etching are studied electrochemically. The CVs of Pd/NiFe-LDH (Figure 4a) and Pd/D-NiFe-LDH (Figure 4b) are acquired in the potential range of 0.2 to 1.6 V vs RHE at different sweeping rates from 1 to 100 mV s^{-1} in 1.0 mol L^{-1} KOH. Compared to the CV curves of NiFe-LDH (Figure S11), the oxidation process of $Ni(OH)_2$ is inhibited after the Pd doping, as shown by the disappearance of the anodic peaks at 1.45 V vs RHE, which overlaps the OER process.[32] After KOH etching, the inhibited oxidation process of $Ni(OH)_2$ would be identified from the disappearance of the anodic peaks at 1.45 V vs RHE and also the reduction peaks at potential 1.4 V vs RHE in the reverse sweep, which shows a negative shifting potential with a low current density compared to Pd/NiFe-LDH. The reducing current density of Pd/D-NiFe-LDH is 33 mA cm^{-2} at a scanning rate of 100 mV s^{-1}, which is lower than that of Pd/NiFe-LDH (58 mA cm^{-2}).

For the cathodic peaks at potential 1.4 V vs RHE, the potentials and current densities versus scanning rates are shown in Figure 4c,d, respectively. For Pd/NiFe-LDH, the potential decreases from 1.47 to 1.39 V vs RHE, while the current density increases quickly from 8 to 40 mA cm^{-2} as the scanning rate goes up from 1 to 40 mV s^{-1}. The potential decreases slowly, and current density is almost constant (∼50 mA cm^{-2}) when the scanning rate is larger than 60 mV s^{-1}. After KOH etching (Pd/D-NiFe-LDH), a similar tendency is observed only with a low potential and current density. The potential decreases from 1.43 to 1.37 V vs RHE when the scanning rate increases from 1 to 40 mV s^{-1} and current density increases from 3 to 24 mA cm^{-2}. When the scanning rates increase from 60 to 100 mV s^{-1}, the potential decreases slowly (from 1.37 to 1.36 V vs RHE), and the current density is almost constant (∼30 mA cm^{-2}). The inhibited redox process of NiFe-LDH after KOH etching results in a negative shift of the reduction peak and decreasing current density.

Compared to the CV curves of NiFe-LDH (Figure S11), the additional reduction peak at 0.7 V vs RHE is attributed to the reduction process of PdO to $Pd(OH)_x$ and then metallic Pd.[23−25] Since $Pd(OH)_x$ and bare Pd have upshifted d-band centers and elongated O−O band distances of intermediates compared to PdO, the ORR is accelerated by the adsorption and dissociation of O_2. The reduction peaks shift to a low potential with scanning rates, and the current density increases to 18 mA cm^{-2} for Pd/NiFe-LDH and 24 mA cm^{-2} for Pd/D-NiFe-LDH at a scanning rate of 100 mV s^{-1}. The current densities and potentials of the reduction peaks at different scanning rates are shown in Figure 4e,f, respectively. For Pd/NiFe-LDH, the potentials decrease from 0.82 to 0.68 V, and current densities increase from 2.5 to 19 mA cm^{-2} when the scanning rate increases from 1 to 40 mV s^{-1}. The potential is almost constant at 0.7 V vs RHE, and the current density decreases slowly to 16 mA cm^{-2} with scanning rates increasing from 40 to100 mV s^{-1}. As for Pd/D-NiFe-LDH, the potential decreases from 0.76 to 0.60 V vs RHE when the scanning rate increases from 1 to 100 mV s^{-1}, and the peak current density increases from 2 to 24 mA cm^{-2} linearly (with a slope of 0.497). To forms nanopores on the electrode surface after etching, the diffusion-determined redox process is identified (slope 0.5),[33,34] and a large reduction current density is obtained at high scanning rates. It indicates that surface

https://doi.org/10.1021/acsaem.5c02043
ACS Appl. Energy Mater. 2025, 8, 12857−12867

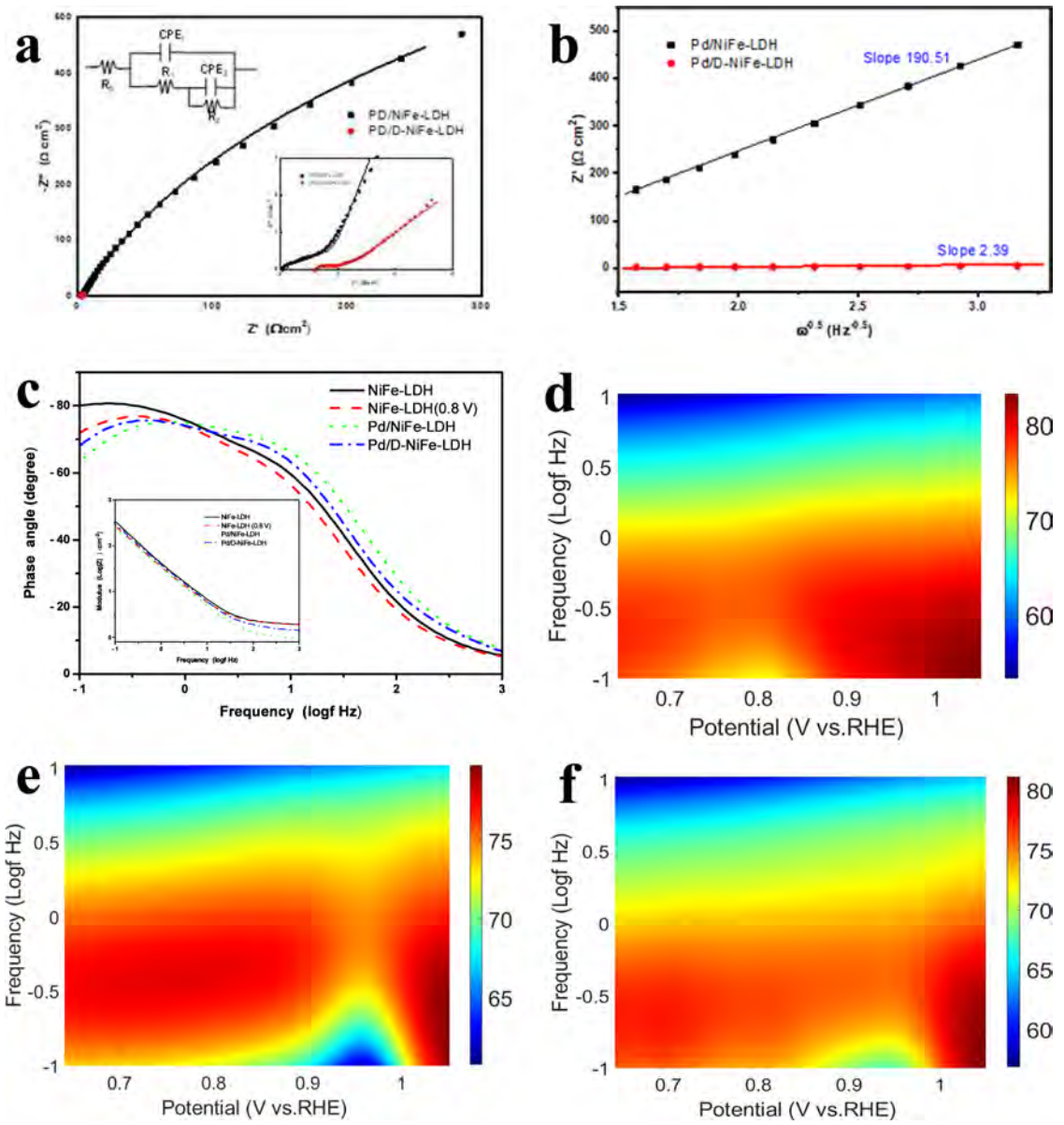

Figure 5. Dynamic EIS at ORR potential region. (a) EIS at OCP including high-frequency region and equivalent-circuit (insets), and also (b) slopes of impedance at low frequency. (c) Phase angles versus frequency at potential 0.95 V vs RHE (also EIS data at 0.8 V vs RHE for NiFe-LDH). Contour pictures of phase angle at low frequency during ORR potential region for (d) NiFe-LDH, (e) Pd/NiFe-LDH, and (f) Pd/D-NiFe-LDH.

etching changes the surface microstructure and electronic states to influence the electrocatalytic properties.

In order to study the kinetic process, electrochemical impedance spectra (EIS) are collected at the OCP in 1.0 mol-L^{-1} KOH, as shown in Figure 5a. In the Nyquist plots, two semicircles appear in the frequency range between 0.1 Hz and 100 kHz. The equivalent circuit is exhibited (inset in Figure 5a) based on the kinetics model of the electrode coated with a porous layer.[35,36] In the equivalent circuit, the constant phase element (CPE) components are introduced to represent the distribution effects of the surface porous network.[35] R_S stands for series resistance. At the surface of the porous electrode, the corresponding impedance is the parallel combination of CPE CPE_1 and charge transfer resistance R_1, corresponding to the semicircle in the high-frequency region. The diffusion-limited ion transfer process can be considered to be CPE_2, which is in parallel with the impedance R_2 and corresponds to the semicircle in the low-frequency region. The good consistency between the experimental data (dots) and fitted data (solid lines) corroborates the validity of the equivalent circuit. According to the fitted results, the series resistance R_S between the electrode/electrolyte interface increases from 2.094 Ω (Pd/NiFe-LDH) to 2.531 Ω cm^2 (Pd/D-NiFe-LDH) after KOH etching. Pd/D-NiFe-LDH shows a small charge transfer resistance R_1 (0.735 Ω cm^2) compared to Pd/D-NiFe-LDH (1.014 Ω cm^2), thereby verifying the fast surface redox processes. CPE_1 represents the pseudocapacitances of the surface processes (including the space charge layer effect and partially redox process). The capacitance effect would be mainly the surface process due to the index n_1 of the constant phase elements approaching unity for Pd/NiFe-LDH (n_1 = 0.851). The diffusion-limited ion transfer process would be the determined process for Pd/D-NiFe-LDH corresponding to the low value of n_1 = 0.5567, which also identifies the fast electrode

https://doi.org/10.1021/acsaem.5c02043
ACS Appl. Energy Mater. 2025, 8, 12857−12867

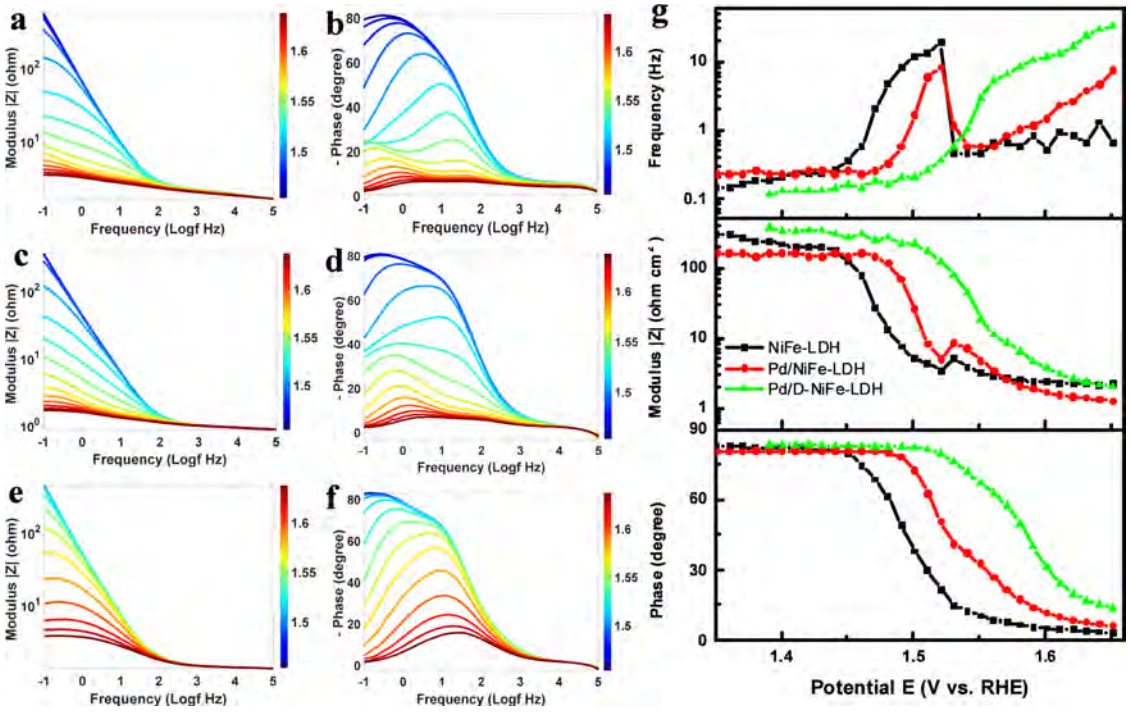

Figure 6. Dynamic EIS at OER potential region. Bode plots with modulus and phase angle for (a,b) NiFe-LDH, (c,d) Pd/NiFe-LDH, and (e,f) Pd/D-NiFe-LDH. (g) Maximum phase angle and related modulus and frequency versus potential at the OER potential region obtained from operando EIS.

redox process on the electrode surface.[35,36] In addition, ion diffusion can also be identified from the relationship between the real part of impedance and low frequencies (Z′ versus $\omega^{-0.5}$, Supporting Information). A smaller slope is observed from Pd/D-NiFe-LDH (2.39) than Pd/NiFe-LDH (190.51) according to the real part of impedance in the low frequency region, indicating fast ion diffusion kinetics after KOH etching.[37−39]

For the Pd-based catalyst, three domains appear during ORR.[23−25] The high potential region corresponds to the activation process, where the reaction rate is limited by the transfer of electrons from the electrocatalyst surface to oxygen. The almost zero current density arises from the weak adsorption energy of oxygen, together with the short O−O bond on oxidized Pd, reducing the higher barrier for oxygen dissociation. The low potential region corresponds to the diffusion-limiting process, where the reaction rate is limited by the mass transport of oxygen from the bulk electrolyte to the active sites. The large reduction current density is attributed to the strong adsorption energy of oxygen together with the elongated O−O bond distance on metallic and hydroxylated Pd, thus reducing the barrier for oxygen dissociation on the electrode surface. The middle potential is the mixed kinetics diffusion-controlled region, which corresponds to the sharp change of the current density from zero to a large one. To understand the electrocatalytic process quantitatively, operando EIS is conducted to identify the interface charge transport and elementary reactions.[40−42] The operando EIS data are acquired using a direct current (DC) step-potential sweep because the EIS overlaps the oscillating alternating current waveform on the DC staircase potential background. EIS data at low-frequency region are interesting to analyze the ORR because that large current density appears at the potential region determined by diffusion-controlled and/or mixed kinetics-diffusion-controlled processes.

The contour pictures of the phase angle at low frequencies (from 0.1 to 10 Hz) are shown during the ORR potential region from 0.62 to 1.05 V vs RHE for NiFe-LDH (Figure 5d), Pd/NiFe-LDH (Figure 5e), and Pd/D-NiFe-LDH (Figure 5f). Figure 5c shows the phase angle and modulus (inset) at low frequencies (from 0.1 to 1000 Hz) at 0.95 V vs RHE for three electrodes. The EIS data of NiFe-LDH at 0.8 V vs RHE is also shown. The electrodes are the blocking systems during the potential region corresponding to the high values of phase angles (>70°) and slopes of lines (−1) for modulus on a logarithmic scale at low frequencies, as shown in Figure 5c.[35] NiFe-LDH (Figure 5d) shows the decreasing phase angles at low frequencies during the potential region from 0.75 to 0.85 V vs RHE (yellow color). For a 3D picture of the phase angle versus potential and frequency, a clear dip is shown at low frequencies, and the low phase angle region extends from 0.1 to 0.3 Hz at 0.8 V vs RHE (Figure S12a). At 0.1 Hz, the phase angle and modulus are 76° and 245 Ω cm^2 at 0.8 V vs RHE, which is lower than the phase angle and modulus (80° and 302 Ω cm^2) at 0.95 V vs RHE, as shown in Figure 5c. After Pd doping (Pd/NiFe-LDH, Figures 5e and S12b), the low value region shifts to a high potential region, and the phase angles decrease to low values, especially from 0.92 to 0.98 V vs RHE (bule color), corresponding to the clearly dip in the 3D picture. As for 0.95 V vs RHE, the phase angle and modulus are 63° and 219 Ω cm^2 at 0.1 Hz. After etching (Pd/D-NiFe-LDH, Figures 5f and S12c), the low value phase angle region also appears at the same potential of 0.95 V vs RHE, and only shifts to the low frequency. Compared to the LSV curves for ORR (Figure 2e), the low phase angle region is related to the onset potential, corresponding to the reaction process of electron transfer from the electrocatalyst surface to oxygen,[23]

https://doi.org/10.1021/acsaem.5c02043
ACS Appl. Energy Mater. 2025, 8, 12857−12867

which is consistent with the sharply increasing current densities in ORR data for Pd/NiFe-LDH and Pd/D-NiFe-LDH. The reaction would be controlled by the diffusion process of oxygen because that electrocatalyst is the blocking system, which corresponds to the decreasing phase angles at low frequency. The ORR process of NiFe-LDH can also be identified, corresponding to the fact that the low-value region of the phase angle is also consistent with the sharply increasing current density at 0.8 V vs RHE. It indicates that the ORR process can be identified by the operando EIS data, especially the phase angles at the low-frequency region.

Due to the approaching potential region for electrooxidation of nickel hydroxide and the OER process, it is difficult to identify the electrochemical redox process by CV curves. Operando EIS can identify the interface charge transport and elementary reaction process during the electrocatalytic process. By analyzing the EIS data, especially the phase angle versus frequency at different potentials, the electrooxidation and OER processes can be identified.[40] To understand the OER mechanism, the modulus and phase angle versus frequency from 1.42 to 1.69 V vs RHE are shown for NiFe-LDH (Figure 6a,b), Pd/NiFe-LDH (Figure 6c,d), and Pd/D-NiFe-LDH (Figure 6e,f), respectively. At low potential, three electrodes are blocking systems corresponding to the high values of phase angle and lines with a slope of −1 for the modulus at low frequencies. With increasing potentials, NiFe-LDH changes from a blocking system to a reactive system corresponding to the decreasing modulus at low frequencies and shifting phase angle peaks to high frequencies. It shows the quick electrochemical reaction process at high potentials corresponds to the decreasing reaction resistance at low frequency (the same series resistance can be obtained from the high-frequency region)[35] and also high-frequency shifting of phase angle peaks with decreasing values. The phase angle peaks shift to the high-frequency region (∼50 Hz), and the values decrease from 80° to 20° when the potential is higher than 1.54 V vs RHE. It reaches ∼10° when the potential is higher than 1.55 V vs RHE (at ∼90 Hz). A new phase angle peak appears at low frequencies (less than 1 Hz) when the potential is higher than 1.55 V vs RHE, and the new peak shifts to a high frequency with decreasing phase angle. The electrodes also change from blocking systems to reaction systems with increasing potentials for Pd/NiFe-LDH and Pd/D-NiFe-LDH, corresponding to a decreasing modulus at low frequencies and shifting phase angle peaks to high frequencies. With regard to Pd/NiFe-LDH (Figure 6c,d), there are two peaks of phase angle versus frequency at low and high frequency, respectively, similar to that of NiFe-LDH. The peaks at low and high frequencies are related to the OER process and electrocatalyst electrooxidation reaction, respectively.[15,40] It indicates that the electrodes change from a blocking system to a reaction system with increasing potentials, and the RDS changes from electrocatalyst electrooxidation to the OER according to the phase angle peaks. However, it cannot be distinguished two peaks clearly in phase angle versus frequency for Pd/D-NiFe-LDH (Figure 6e,f).

To analyze the dynamic reaction process quantitatively, the maximum values of phase angles at different potentials are selected to study the RDS changing from electrocatalyst electrooxidations to the OER. The related modulus and frequencies are also obtained, as shown in Figure 6g. Three electrodes are the blocking systems at low potentials corresponding to large phase angle and modulus, as well as low frequency. With increasing potential, three electrodes change from blocking systems to reactive systems at potential 1.45, 1.49, and 1.51 V vs RHE for NiFe-LDH, Pd/NiFe-LDH, and Pd/D-NiFe-LDH, respectively, corresponding to the decreasing phase angle and modulus and increasing frequency. For NiFe-LDH, the phase angle decreases from 83° to 15°, the related modulus decreases from 260 to 3 Ω cm^2, and the frequency increases from 0.2 to 20 Hz during the potential increase from 1.45 to 1.52 V vs RHE. The frequency decreases sharply from 20 to 0.4 Hz at 1.53 V vs RHE, and then three parameters show small changes with increasing potentials, corresponding to the slow decreasing of phase angles and modulus and almost constant values of frequencies. For Pd/NiFe-LDH, the phase angle decreases from 80 to 41°, the related modulus decreases from 160 to 5 Ω cm^2, and the frequency increases from 0.2 to 8 Hz during potential increases from 1.49 to 1.52 V vs RHE. The frequency also decreases sharply from 8 to 0.5 Hz at 1.54 V vs RHE. With increasing potentials from 1.54 to 1.65 V vs RHE, it shows the quickly increasing frequency and reaches 5 Hz at 1.65 V vs RHE. It also shows the quickly decreasing phase angle and modulus compared to NiFe-LDH. Pd/D-NiFe-LDH shows simply decreasing phase angles and modulus and increasing frequencies when the potential is higher than 1.52 V vs RHE.

Related to the electrochemical process during the OER potential region, it indicates that the electrooxidation reaction of NiFe-LDH begins at 1.45 V vs RHE, corresponding to the decreasing phase angle and modulus and also increasing frequency. The decreasing frequency at 1.52 V vs RHE is related to the RDS changing from electrooxidation to OER. With increasing potential, the almost constant frequency and slowly decreasing phase angle and modulus indicate a sluggish OER process on the NiFe-LDH electrode,[40] which is also identified from the LSV data (Figure 2e). The electrooxidation reaction of NiFe-LDH could not be inhibited after the Pd-doping process (Pd/NiFe-LDH) and only shifts to a high potential 1.49 V vs RHE. The OER process is the RDS after 1.53 V vs RHE and shows improved OER performance corresponding to the increasing frequency and also decreasing phase angle and modulus with the increasing potential, which can also be identified from the LSV data (Figure 2e). After the etching process (Pd/D-NiFe-LDH), the electrooxidation reaction of NiFe-LDH is totally inhibited as manifested by the disappearance of decreasing frequency. The decreasing phase angle and modulus and also increasing frequency at 1.51 V vs RHE are related to the beginning of the OER, which also can be identified from the LSV data (Figure 2e). It indicates that the KOH etching process stabilizes OER by limiting the electrooxidation of NiFe-LDH ($Ni^{2+} - OH + OH^- = e^- + Ni^{3+}$-$O + H_2O$).[40] Owing to the inhibited oxidation of NiFe-LDH, the reduction of $PdOH_x$ to metallic Pd shifts to the negative potential and reduces the high current density of ORR. The hybrid Ni−Zn and ZABs are formed to enhance the performance of battery, including the high open-circuit voltage, reversibility, and stability.

3. CONCLUSION

Hierarchical porous defective Pd-doped NiFe-LDH is fabricated on conductive CC by electrodeposition and alkaline etching to form a high-performance bifunctional catalyst (ORR/OER) for a Zn−air battery. The Zn−air battery shows high reversibility and stability on account of the larger surface area of the hierarchical porous structure and the

https://doi.org/10.1021/acsaem.5c02043
ACS Appl. Energy Mater. 2025, 8, 12857−12867

modulated surface electronic states after etching. Electrochemical assessment by CV and electrochemical impedance spectroscopy is carried out to investigate the surface electronic states. Operando EIS reveals the ORR process based on the phase angle versus potential results at low frequencies. The Operando EIS data also distinguish electrooxidation from the oxidation of the oxygen species (OER) and are used to identify inhibited electrooxidation of Pd-doped NiFe-LDH after alkaline etching. The inhibited oxidation of NiFe-LDH improves the performance of the battery through the formation of a hybrid Ni−Zn and Zn−air battery. The results reveal that the surface structure and electronic states are crucial to the performance and stability of bifunctional ORR/OER electrodes.

■ ASSOCIATED CONTENT

Supporting Information

The Supporting Information is available free of charge at https://pubs.acs.org/doi/10.1021/acsaem.5c02043.

Experimental details, material characterization (XRD and Raman spectra), catalytic properties of Pd/D-NiFe-LDH with different Pd constituents and etching times, XPS spectra, electrochemical analysis (CV and LSV curves), performance of ZABs, cyclability of different ZABs, and electrochemical analysis (CV curves, 3D pictures of phase angle versus frequency in ORR potential region) (PDF)

■ AUTHOR INFORMATION

Corresponding Authors

Shaohui Xu − *Key Laboratory of Polar Materials and Devices, Ministry of Education, and School of Physics and Electronic Science, East China Normal University, Shanghai 200241, China; Department of Physics, Department of Materials Science & Engineering, and Department of Biomedical Engineering, City University of Hong Kong, Kowloon, Hong Kong 999077, China;* orcid.org/0000-0002-8201-0354; Email: shxu@ee.ecnu.edu.cn

Zhenzhong Yang − *Key Laboratory of Polar Materials and Devices, Ministry of Education, and School of Physics and Electronic Science, East China Normal University, Shanghai 200241, China;* orcid.org/0000-0002-7226-7973; Phone: +86 21 54342501; Email: zzyang@phy.ecnu.edu.cn; Fax: +86 21 54345119

Authors

Beibei Wang − *Key Laboratory of Polar Materials and Devices, Ministry of Education, and School of Physics and Electronic Science, East China Normal University, Shanghai 200241, China*

Youyuan Zhang − *Key Laboratory of Polar Materials and Devices, Ministry of Education, and School of Physics and Electronic Science, East China Normal University, Shanghai 200241, China*

Dajun Wu − *Jiangsu Laboratory of Advanced Functional Materials, School of Electronic and Information Engineering, Suzhou University of Technology, Changshu 215500, China*

Fanya Jin − *Southwest Institute of Physics of Nuclear Industry, Chengdu 610041, China*

Dayuan Xiong − *Key Laboratory of Polar Materials and Devices, Ministry of Education, and School of Physics and Electronic Science, East China Normal University, Shanghai 200241, China*

Lianwei Wang − *Key Laboratory of Polar Materials and Devices, Ministry of Education, and School of Physics and Electronic Science, East China Normal University, Shanghai 200241, China;* orcid.org/0000-0001-6368-660X

Paul K. Chu − *Department of Physics, Department of Materials Science & Engineering, and Department of Biomedical Engineering, City University of Hong Kong, Kowloon, Hong Kong 999077, China;* orcid.org/0000-0002-5581-4883

Complete contact information is available at: https://pubs.acs.org/10.1021/acsaem.5c02043

Author Contributions

⊥B.W. and Y.Z. contributed equally.

Notes

The authors declare no competing financial interest.

■ ACKNOWLEDGMENTS

This work was jointly supported by the National Natural Science Foundation of China (No. 61176108), the Research Innovation Foundation of ECNU (No. 78210245), and the City University of Hong Kong Donation Research Grants (DON-RMG Nos. 9229021 and 9220061).

■ REFERENCES

(1) Zhu, Z.; Jiang, T.; Ali, M.; Meng, Y.; Jin, Y.; Cui, Y.; Chen, W. Rechargeable Batteries for Grid Scale Energy Storage. *Chem. Rev.* **2022**, *122*, 16610−16751.

(2) Lee, J.-S.; Kim, S. T.; Cao, R.; Choi, N.-S.; Liu, M.; Lee, K. T.; Cho, J. Metal-Air Batteries with High Energy Density: Li-Air versus Zn-Air. *Adv. Energy Mater.* **2011**, *1*, 34−50.

(3) Wang, M.; Zhang, L.; He, Y.; Zhu, H. Recent advances in transition-metal-sulfide-based bifunctional electrocatalysts for overall water splitting. *J. Mater. Chem. A* **2021**, *9*, 5320−5363.

(4) Fu, J.; Cano, Z. P.; Park, M. G.; Yu, A.; Fowler, M.; Chen, Z. Electrically Rechargeable Zinc-Air Batteries: Progress, Challenges, and Perspectives. *Adv. Mater.* **2017**, *29* (7), 1604685.

(5) Zhou, T.; Zhang, N.; Wu, C.; Xie, Y. Surface/interface nanoengineering for rechargeable Zn-air batteries. *Energy Environ. Sci.* **2020**, *13*, 1132−1153.

(6) Liu, Q.; Wang, L.; Fu, H. Research progress on the construction of synergistic electrocatalytic ORR/OER self-supporting cathodes for zinc-air batteries. *J. Mater. Chem. A* **2023**, *11*, 4400−4427.

(7) Liu, G.; Nie, T.; Song, Z.; Sun, X.; Shen, T.; Bai, S.; Yu, T.; Zheng, L.; Song, Y. Pd-Embedded NiFe Layered Double Hydroxides for Biomass Upgrading: Precision Construction of Dual-Functional Synergistic Sites. *Adv. Funct. Mater.* **2024**, *34* (52), 2411284.

(8) Zhong, X.; Xiao, X.; Li, Q.; Zhang, M.; Li, Z.; Gao, L.; Chen, B.; Zheng, Z.; Fu, Q.; Wang, X.; Zhou, G.; Xu, B. Understanding the active site in chameleon like bifunctional catalyst for practical rechargeable zinc-air batteries. *Nat. Commun.* **2024**, *15*, 9616.

(9) Wang, D.; Li, F.; Liu, M.; Lu, G.; Cheng, H. 3D Aperiodic Hierarchical Porous Graphitic Carbon Material for High-Rate Electrochemical Capacitive Energy Storage. *Angew. Chem., Int. Ed.* **2008**, *47*, 373−376.

(10) He, Y.; Yang, J.; Wang, Y.; Jia, Y.; Li, H.; Liu, Y.; Liu, L.; Tan, Q. Atomically Dispersed Dual-Metal ORR Catalyst with Hierarchical Porous Structure for Zn-Air Batteries. *ACS Appl. Mater. Interface* **2024**, *16*, 12398−12406.

(11) Wang, L.; Huang, K.; Chen, J.; Zheng, J. Ultralong cycle stability of aqueous zinc-ion batteries with zinc vanadium oxide cathodes. *Sci. Adv.* **2019**, *5* (10), No. eaax4279.

(12) Wang, Y.; Zhu, Y.; Zhao, S.; She, S.; Zhang, F.; Chen, Y.; Williams, T.; Gengenbach, T.; Zu, L.; Mao, H.; et al. Anion Etching

for Accessing Rapid and Deep Self-Reconstruction of Precatalysts for Water Oxidation. *Matter* **2020**, *3*, 2124−2137.
(13) Cho, K.; Park, S.; Nam, K. Engineered Dissolution for Better Electrocatalysts. *Chem.* **2021**, *7*, 20−21.
(14) Liu, H.; Wang, Y.; Lu, X.; Hu, Y.; Zhu, G.; Chen, R.; Ma, L.; Zhu, H.; Tie, Z.; Liu, J.; et al. The effects of Al substitution and partial dissolution on ultrathin NiFeAl trinary layered double hydroxide nanosheets for oxygen evolution reaction in alkaline solution. *Nano Energy* **2017**, *35*, 350−357.
(15) Fan, J.; Jiang, J.; Wang, Y.; Zhang, X.; Liu, Y.; Yang, X.; Pan, T.; Xu, D.; Shi, N.; Lin, Y.; Han, M.; Pang, H. Etching Accelerates Reconstruction and Activates Lattice Oxygen of Anion Vacancies-Enriched Cobalt-Iron Phosphide/(Oxy)Hydroxide Nanohybrid Frameworks for Enhanced Oxygen Evolution. *Adv. Funct. Mater.* **2025**, No. 1 to 15, 2425770.
(16) Dai, W.; Wan, K.; Pang, K.; Guo, J.; Liu, S.; Wu, K.; Tang, C.; Sun, Y.; Shi, X.; Tang, Z.; et al. In-depth understanding and precise modulation of surface reconstruction during heterogeneous electrocatalysis: From model to practical catalyst. *Chem.* **2025**, *11* (1), 102345.
(17) Zhai, P.; Xia, M.; Wu, Y.; Zhang, G.; Gao, J.; Zhang, B.; Cao, S.; Zhang, Y.; Li, Z.; Fan, Z.; et al. Engineering single-atomic ruthenium catalytic sites on defective nickel-iron layered double hydroxide for overall water splitting. *Nat. Commun.* **2021**, *12*, 4587.
(18) Bai, L.; Lee, S.; Hu, X. Spectroscopic and Electrokinetic Evidence for a Bifunctional Mechanism of the Oxygen Evolution Reaction. *Angew. Chem., Int. Ed.* **2021**, *60*, 3095−3103.
(19) Zou, C.; Liu, W.; Chen, S.; Xu, Y.; Tang, Y.; Li, S.; Yang, F.; Yu, L.; Zeng, C.; Zhang, Y. Y.; et al. Two Distinct Oxidation Dispersion Mechanisms in Pd-CeO_2 Mediated by Thermodynamic and Kinetic Behaviors of Highly Dispersed Pd Species. *Phys. Rev. Lett.* **2025**, *134*, 218001.
(20) Yue, S.; Praveen, C. S.; Klyushin, A.; Fedorov, A.; Hashimoto, M.; Li, Q.; Jones, T.; Liu, P.; Yu, W.; Willinger, M. G.; et al. Redox dynamics and surface structures of an active palladium catalyst during methane oxidation. *Nat. Commun.* **2024**, *15*, 4678.
(21) Zhang, N.; Feng, X.; Rao, D.; Deng, X.; Cai, L.; Qiu, B.; Long, R.; Xiong, Y.; Lu, Y.; Chai, Y. Lattice oxygen activation enabled by high-valence metal sites for enhanced water oxidation. *Nat. Commun.* **2020**, *11*, 4066.
(22) He, Z.; Zhang, J.; Gong, Z.; Lei, H.; Zhou, D.; Zhang, N.; Mai, W.; Zhao, S.; Chen, Y. Activating lattice oxygen in NiFe-based (oxy) hydroxide for water electrolysis. *Nat. Commun.* **2022**, *13*, 2191.
(23) Wang, Q.; Guesmi, H.; Tingry, S.; Cornu, D.; Holade, Y.; Minteer, S. D. Unveiling the Pitfalls of Comparing Oxygen Reduction Reaction Kinetic Data for Pd-Based Electrocatalysts without the Experimental Conditions of the Current-Potential Curves. *ACS Energy Lett.* **2022**, *7*, 952−957.
(24) Qiao, S.; Shou, H.; Xu, W.; Cao, Y.; Zhou, Y.; Wang, Z.; Wu, X.; He, Q.; Song, L. Regulating and identifying the structures of PdAu alloys with splendid oxygen reduction activity for rechargeable zinc-air batteries. *Energy Environ. Sci.* **2023**, *16*, 5842−5851.
(25) Lin, F.; Lv, F.; Zhang, Q.; Luo, H.; Wang, K.; Zhou, J.; Zhang, W.; Zhang, W.; Wang, D.; Gu, L.; et al. Local Coordination Regulation through Tuning Atomic-Scale Cavities of Pd Metallene toward Efficient Oxygen Reduction Electrocatalysis. *Adv. Mater.* **2022**, *34* (27), 2202084.
(26) Xing, W.; Yin, G.; Zhang, J. *Rotating Electrode Methods and Oxygen Reduction Electrocatalysts*; Elsevier: Waltham, MA, 2014.
(27) Li, Y.; Huang, A.; Zhou, L.; Li, B.; Zheng, M.; Zhuang, Z.; Chen, C.; Chen, C.; Kang, F.; Lv, R. Main-group element-boosted oxygen electrocatalysis of Cu-N-C sites for zinc-air battery with cycling over 5000 h. *Nat. Commun.* **2024**, *15*, 8365.
(28) Chung, D.; Lopes, P. P.; Farinazzo Bergamo Dias Martins, P.; He, H.; Kawaguchi, T.; Zapol, P.; You, H.; Tripkovic, D.; Strmcnik, D.; Zhu, Y.; Seifert, S.; Lee, S.; Stamenkovic, V. R.; Markovic, N. M. Dynamic stability of active sites in hydr(oxy)oxides for the oxygen evolution reaction. *Nat. Energy* **2020**, *5*, 222−230.
(29) Kuang, M.; Zheng, G. Nanostructured bifunctional redox electrocatalysts. *Small* **2016**, *12*, 5656−5675.
(30) Parker, J. F.; Chervin, C. N.; Pala, I. R.; Machler, M.; Burz, M. F.; Long, J. W.; Rolison, D. R. Rechargeable nickel-3D zinc batteries: An energy-dense, safer alternative to lithium-ion. *Science* **2017**, *356*, 415−418.
(31) Lee, D. U.; Fu, J.; Park, M. G.; Liu, H.; Ghorbani Kashkooli, A.; Chen, Z. Self-Assembled NiO/$Ni(OH)_2$ Nanoflakes as Active Material for High Power and High-Energy Hybrid Rechargeable Battery. *Nano Lett.* **2016**, *16*, 1794−1802.
(32) Barral, G.; Njanjo-Eyoke, F.; Maximovitch, S. Characterization of the passive layer and of hydroxide deposits of nickel by impedance spectroscopy. *Electrochim. Acta* **1995**, *40*, 2815−2828.
(33) Bard, A. J.; Larry, R. *Electrochemical Methods: Fundamentals and Applications*; John Wiley & Sons, Inc: New York, 2001.
(34) Augustyn, V.; Come, J.; Lowe, M. A.; Kim, J. W.; Taberna, P.-L.; Tolbert, S. H.; Abruna, H. D.; Simon, P.; Dunn, B. High-rate electrochemical energy storage through Li^+ intercalation pseudocapacitance. *Nat. Mater.* **2013**, *12*, 518−522.
(35) Orazem, M. E.; Tribollrt, B. *Electrochemical Impedance Spectroscopy*; John Wiley & Sons, Inc: New Jersey, Hoboken, 2008.
(36) Lyons, M. E. G.; Brandon, M. P. The significance of electrochemical impedance spectra recorded during active oxygen evolution for oxide covered Ni, Co and Fe electrodes in alkaline solution. *J. Electroanal. Chem.* **2009**, *631*, 62−70.
(37) Zheng, J.; Zhu, G.; Liu, X.; Xie, H.; Lin, Y.; Zeng, Y.; Zhang, Y.; Gandi, A. N.; Qi, Z.; Wang, Z.; Liang, H. Simultaneous Dangling Bond and Zincophilic Site Engineering of SiN_x Protective Coatings toward Stable Zinc Anodes. *ACS Energy Lett.* **2022**, *7* (12), 4443−4450.
(38) Deng, S.; Tie, Z.; Yue, F.; Cao, H.; Yao, M.; Niu, Z. Rational Design of $ZnMn_2O_4$ Quantum Dots in a Carbon Framework for Durable Aqueous Zinc-Ion Batteries. *Angew. Chem., Int. Ed.* **2022**, *61* (12), No. e202115877.
(39) Chou, S.; Wang, J.; Liu, H.; Dou, S. Rapid Synthesis of $Li_4Ti_5O_{12}$ Microspheres as Anode Materials and Its Binder Effect for Lithium-Ion Battery. *J. Phys. Chem. C* **2011**, *115*, 16220−16227.
(40) Chen, W.; Wu, B.; Wang, Y.; Zhou, W.; Li, Y.; Liu, T.; Xie, C.; Xu, L.; Du, S.; Song, M.; et al. Deciphering the alternating synergy between interlayer Pt single-atom and NiFe layered double hydroxide for overall water splitting. *Energy Environ. Sci.* **2021**, *14*, 6428−6440.
(41) Luo, W.; Tian, H.; Li, Q.; Meng, G.; Chang, Z.; Chen, C.; Shen, R.; Yu, X.; Zhu, L.; Kong, F.; Cui, X.; Shi, J. Controllable Electron Distribution Reconstruction of Spinel $NiCo_2O_4$ Boosting Glycerol Oxidation at Elevated Current Density. *Adv. Funct. Mater.* **2024**, *34* (3), 2306995.
(42) Seenivasan, S.; Kim, M.; Han, J. W.; Seo, J. Programmed electrochemical reconstruction of $NiCo_xMo_{4-x}N_5$ for making Core-Shell shaped Schottky junction electrocatalyst. *Chem. Eng. J.* **2024**, *497*, 154473.

https://doi.org/10.1021/acsaem.5c02043
ACS Appl. Energy Mater. 2025, 8, 12857−12867

Supporting Information

Modulation of Surface Structure and Electronic States of Defective Pd-Doped NiFe Layered Double Hydroxide Bifunctional Electrocatalyst by Alkaline Etching for Zn-Air Batteries

Beibei Wang[a,1], Youyuan Zhang[a,1], Dajun Wu[b], Fanya Jin[c], Zhenzhong Yang[a*], Shaohui Xu[a,d*], Dayuan Xiong [a], Lianwei Wang[a], and Paul K. Chu[d]

[a] Key Laboratory of Polar Materials and Devices, Ministry of Education, and School of Physics and Electronic Science, East China Normal University, 500 Dongchuan Road, Minhang District, Shanghai, 200241, China

[b] Jiangsu Laboratory of Advanced Functional Materials, School of Electronic and Information Engineering, Suzhou University of Technology, Changshu 215500, China

[c] Southwest Institute of Physics of Nuclear Industry, Chengdu, 610041, China

[d] Department of Physics, Department of Materials Science & Engineering, and Department of Biomedical Engineering, City University of Hong Kong, Tat Chee Avenue, Kowloon, Hong Kong, 999077, China

*Authors to whom correspondence should be addressed:

shxu@ee.ecnu.edu.cn (Shaohui Xu); zzyang@phy.ecnu.edu.cn (Zhenzhong Yang);

Tel.: +86 21 54342501; Fax: +86 21 54345119

Contents

Experimental details

The analytical grade chemicals were purchased from Sinopharm Chemical Reagent Co., Ltd. and used without purification. The aqueous solutions were prepared with deionized (DI) water (18.2 MΩ cm).

1. Synthesis of Pd-D-NiFe-LDH

The carbon cloth (CC) was pretreated by an acid-oxidation method to remove impurities and oil stains. The electrolyte contained 0.12 mmol Ni $(NO_3)_2 \cdot 6H_2O$, 0.12 mmol $Fe(NO_3)_3 \cdot 9H_2O$, 1.0 mmol $Al(NO_3)_3 \cdot 9H_2O$ and 0.028-0.28 mmol $PdCl_2$ in 100 mL DI water. Constant-potential electrodeposition was conducted at -1.0 V vs. Ag/AgCl for 30 min. to obtain the precursor of Pd-doped NiFeAl-LDH (denoted as Pd/NiFe-LDH). Pd/NiFe-LDH was immersed in a 5 mol L^{-1} KOH solution under stirring for 12, 24, and 36 hours. After alkaline etching, the samples were washed thoroughly with deionized water and dried for 6 hours at 60°C to obtain the defective Pd-dopped NiFe-LDH (denoted as Pd/D-NiFe-LDH). For comparison, D-NiFe-LDH (NiFe-LDH) was synthesized by the same procedures with (without) alkaline etching using a similar solution without $PdCl_2$.

2. Materials characterization

The crystal structure was determined by X-ray diffractometer (XRD) with Cu K_α radiation (k = 1.5406 Å). The morphology and composition of the samples were

characterized by field-emission scanning electron microscopy (FE-SEM, Hitachi S-4800, Japan), and the surface chemical compositions were determined by X-ray photoelectron spectroscopy (XPS) with Al K_α irradiation. Transmission electron microscopy (TEM) was conducted to examine the fine structure, and Raman scattering was performed to analyze the vibrational modes using a 514 nm laser. The specific surface area and pore size distributions were determined on the Micromeritics ASAP 2020 N_2 adsorption analyzer.

3. Electrochemical characterizations

The electrochemical analysis was carried out using three-electrode system in 1 mol L^{-1} KOH sulution (Bio-Logic VMP3). The reference and counter electrodes were SCE and Pt plate. Cyclic voltammetry (CV) was performed at scanning rates between 10 and 100 mV s^{-1}. Electrochemical impedance spectroscopy (EIS) was carried out in the frequency range from 100 mHz to 100 kHz along with an alternating current (AC) bias of 10 mV at the open-circuit potential (OCP) or changing potentials from 0 to 1.2 V vs. RHE. Linear sweep voltammetry (LSV) was conducted to assess the ORR and OER activity. The reversible hydrogen electrode (RHE) was evaluated according to the following equation:

$$E_{RHE} = \mathrm{E_0} + 0.059\mathrm{pH} + \mathrm{E(SCE)} \ , \qquad \text{(S1)}$$

where E_0 is 0.2412 V (SCE), pH = 13.6 for 1.0 mol L^{-1} KOH, and E is the working voltage (V). All the measurements were performed at room temperature (25 °C), and the results were normalized to the footprint area.

The polarization curves for ORR were recorded at room temperature in the O_2-saturated 0.1 mol L^{-1} KOH solution at 400-2,500 rpm. In the current-time chronoamperometric test, O_2 was bubbled into the 0.1 mol L^{-1} KOH electrolyte for 30 min, and O_2 was maintained over the electrolyte during the test to ensure oxygen saturation. In the preparation of the ORR working electrode, the polished sample (5 mg) was dispersed ultrasonically in a solution containing ethanol and 5% Nafion to form the ink (5 μL), which was dropped onto the glassy carbon electrode (diameter of 4 mm) and dried naturally for the ORR measurements. The mass of the catalyst deposited on the electrode was 0.4 mg cm^{-2}.

The transfer electron number (n) of the ORR was calculated according to the Koutecky-Levich equation [1, 2]:

$$\frac{1}{J} = \frac{1}{J_L} + \frac{1}{J_K} = \frac{1}{B\omega^{1/2}} + \frac{1}{J_K} \quad \text{and} \quad \text{(S2)}$$

$$B = 0.62nFC_0D_0^{2/3}V^{-1/6} \quad , \quad \text{(S3)}$$

where J is the measured current density, J_K and J_L are the charge transfer kinetics and the diffusion-limited current densities, respectively, ω stands for the angular velocity of the rotating electrode (rad·s^{-1}), n is the electron-transfer number in ORR, F is the Faraday constant (96,485 C·mol^{-1}), C_0 is the bulk concentration of oxygen, D_0 is the diffusion coefficient of oxygen, and V is the kinematic viscosity of the electrolyte. C_0, D_0, and V in 0.1 mol L^{-1} KOH electrolyte were 1.2 × 10^{-6} mol·cm^{-3}, 1.9 ×10^{-5} cm^2·s^{-1} and 0.01 cm^2·s^{-1}, respectively [2].

The ion diffusion process was studied by EIS. According to the low-frequency EIS plots, the ion diffusion coefficients are expressed by the following equation [3-5] :

$$Z' = R_S + R_f + R_{ct} + \sigma_w \omega^{-0.5} \quad \text{(S4)}$$

$$D = \frac{R^2T^2}{2A^2n^4F^4C^2\sigma_w^2} \quad , \quad \text{(S5)}$$

where ω, A, n, F, C, R, and T are the angular frequency, electrode area, reactive electron number per chemical formula, Faraday's constant, molar concentration of ions, gas constant, and room temperature, respectively, and σ_w is the linear slope derived from the relationship between frequencies and real part of the impedance. A small linear slope σ_w corresponds to a high diffusion coefficient.

4. Fabrication of liquid Zn-air battery and measurement

The liquid Zn-air battery was fabricated on a home-made instrument under ambient atmospheric conditions. The catalyst ink was prepared by sonicating the mixture comprising the catalyst (5.0 mg), Nafion solution (5.0 wt.%, 40 μL), and solvent (1000 μL, water/ethanol = 1:3, v/v) for several hours until a homogeneous suspension was formed. Afterward, a certain amount of the catalyst ink (200 μL) was coated and dried on the carbon paper (mass load 1 mg cm^{-2}). The Zn-air battery was composed of the cathode (catalyst-coated carbon paper, area 1 × 1 cm^2), anode (a zinc plate, area 1 × 1 cm^2), and electrolyte (6 mol L^{-1} KOH and 0.2 mol L^{-1} zinc acetate ($Zn(AC)_2$)). The constant current charging/discharging curves were recorded on the LAND battery testing system (Wuhan, China).

References

[1] Xing, W.; Yin G.; Zhang, J. Rotating electrode methods and oxygen reduction electrocatalysts, by Waltham, MA, Elsevier, **2014**.

[2] Li, Y.; Huang, A.; Zhou, L.; Li, B.; Zheng, M.; Zhuang, Z.; Chen, C.; Chen, C.; Kang, F.; Lv, R. Main-group element-boosted oxygen electrocatalysis of Cu-N-C sites for zinc-air battery with cycling over 5000 h, *Nat. Commun.,* **2024**, 15, 8365.

[3] Zheng, J.; Zhu, G.; Liu, X.; Xie, H.; Lin, Y.; Zeng, Y.; Zhang, Y.; Gandi, A. N.; Qi, Z.; Wang, Z.; Liang, H. Simultaneous Dangling Bond and Zincophilic Site Engineering of SiN_x Protective Coatings toward Stable Zinc Anodes, *ACS Energy Lett.*, **2022**, 7(12), 4443-4450.

[4] Deng, S.; Tie, Z.; Yue, F.; Cao, H.; Yao, M.; Niu, Z. Rational Design of $ZnMn_2O_4$ Quantum Dots in a Carbon Framework for Durable Aqueous Zinc-Ion Batteries, *Angew. Chem. Int. Ed.*, **2022**, 61, e202115877 (1 to 6)

[5] Chou, S.; Wang, J.; Liu, H.; Dou, S. Rapid Synthesis of $Li_4Ti_5O_{12}$ Microspheres as Anode Materials and Its Binder Effect for Lithium-Ion Battery, *J. Phys. Chem. C*, **2011**, 115, 16220-16227.

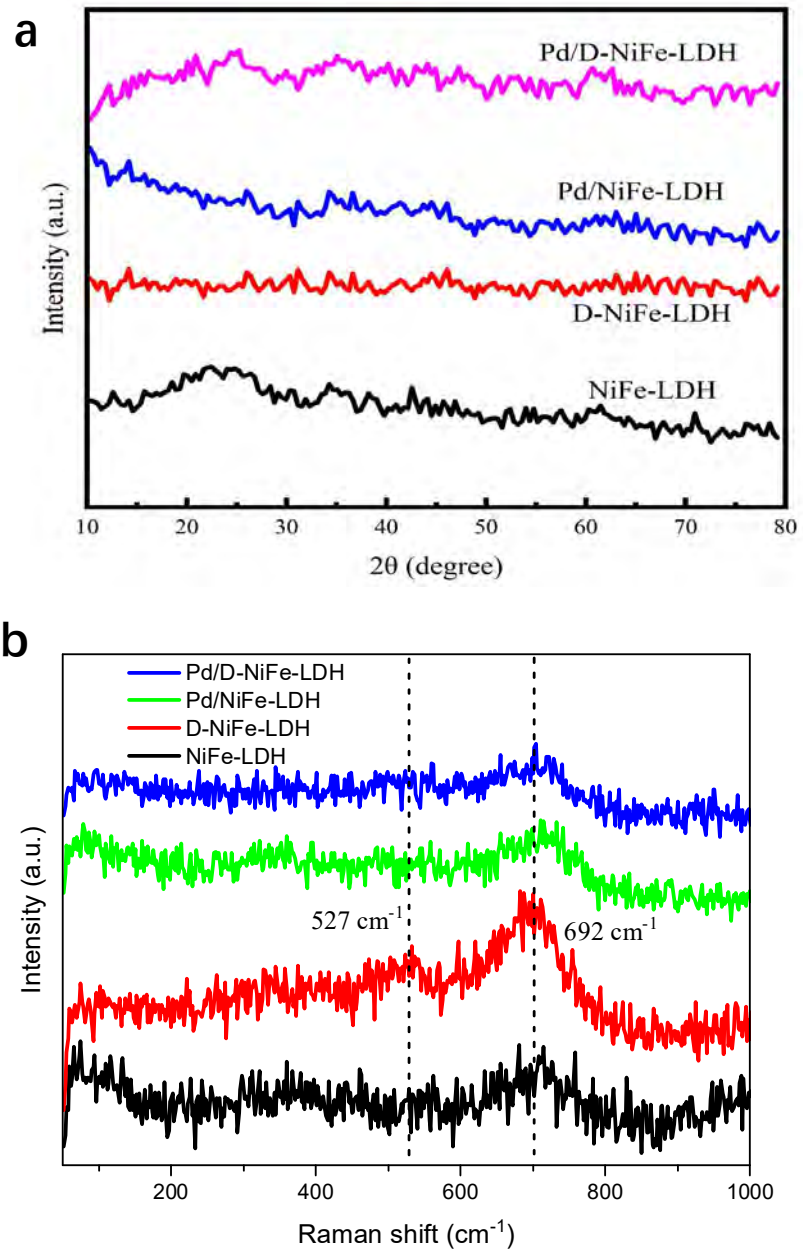

Figure S1. Characterizations of electrodes: (a) XRD patterns and (b) Raman spectra.

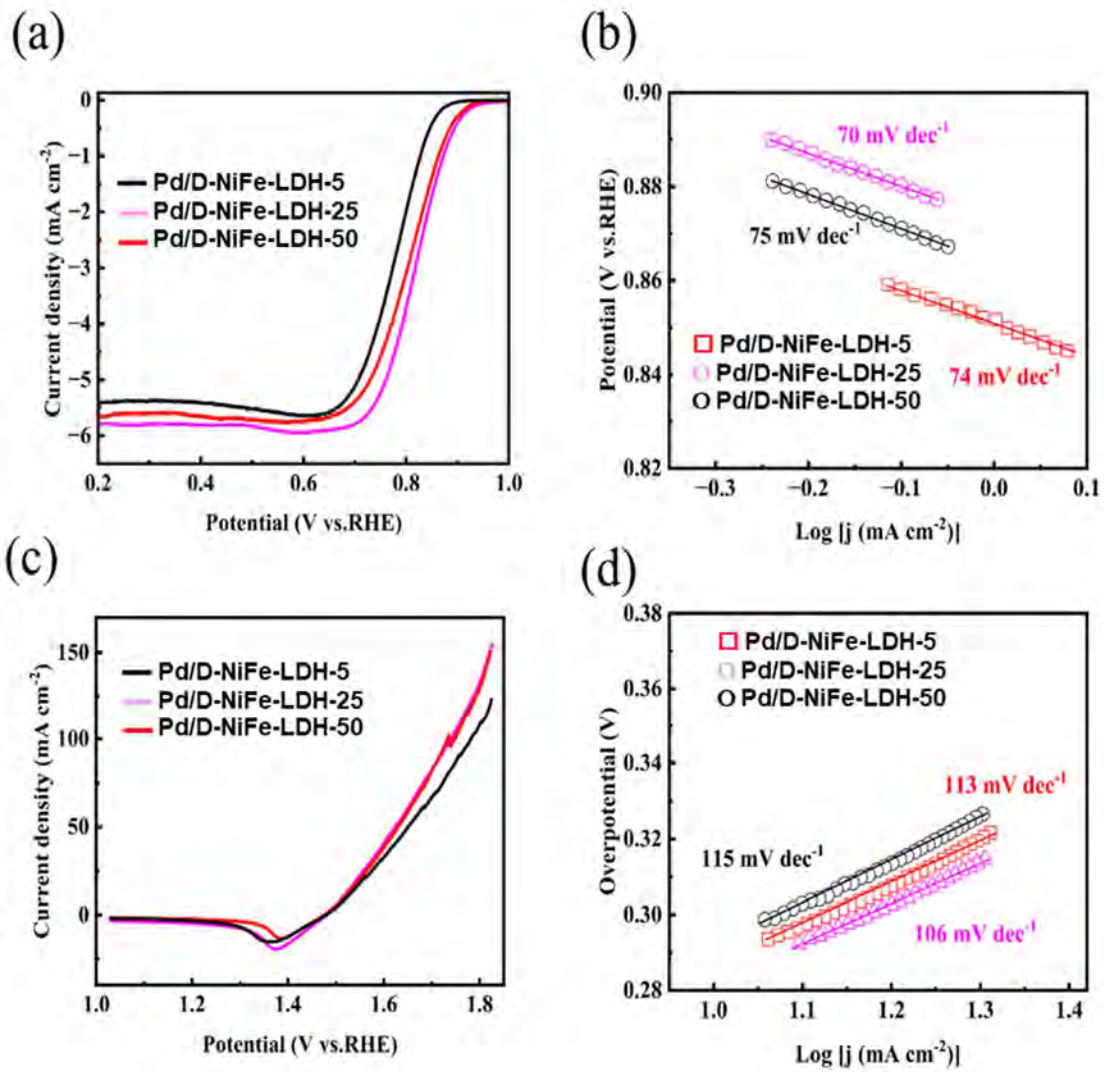

Figure S2. Bifunctional catalytic properties of Pd/D-NiFe-LDH with different Pd concentrations (mass of $PdCl_2$ in mg, 100 mL DI water): (a) ORR and (b)Tafel plots; (c) OER and (d) Tafel plots

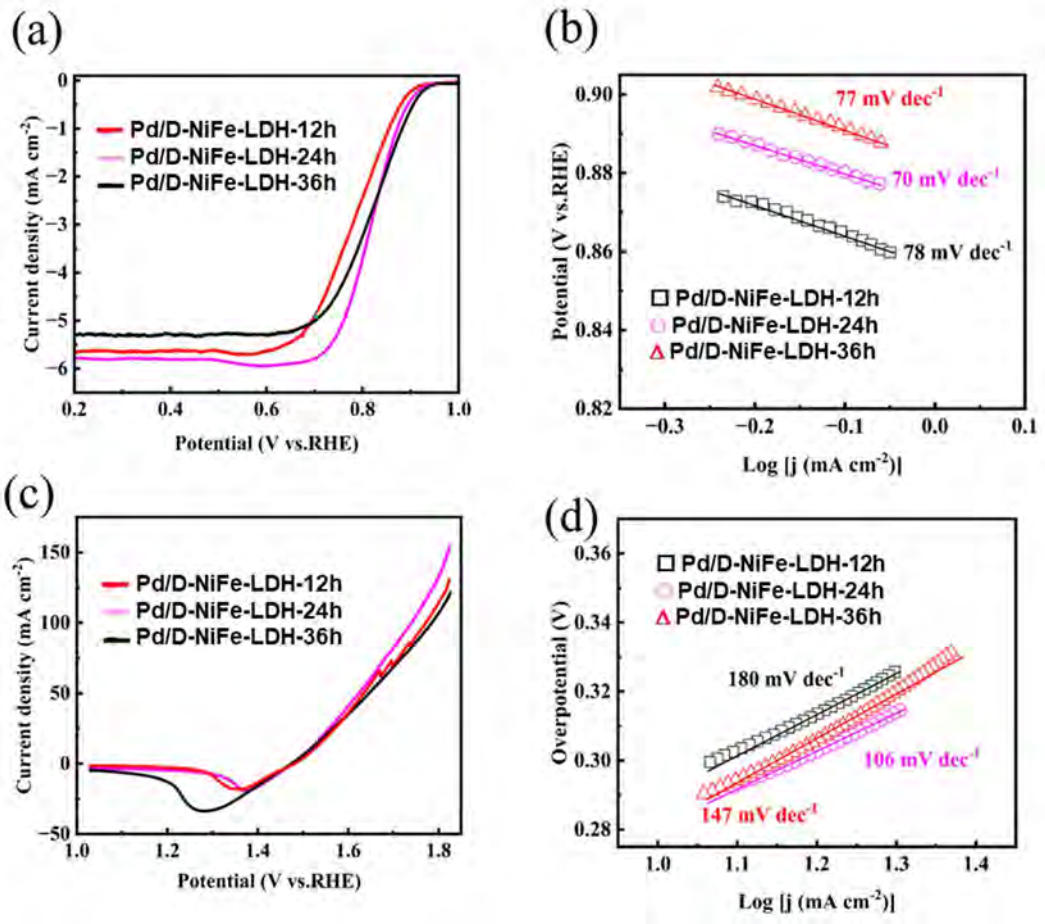

Figure S3. Bifunctional catalytic properties of Pd/D-NiFe-LDH for different etching times in 5 mol L^{-1} KOH solution (25 mg of $PdCl_2$ in 100 mL DI water): (a) ORR and (b) Tafel plots; (c) OER and (d)Tafel plots

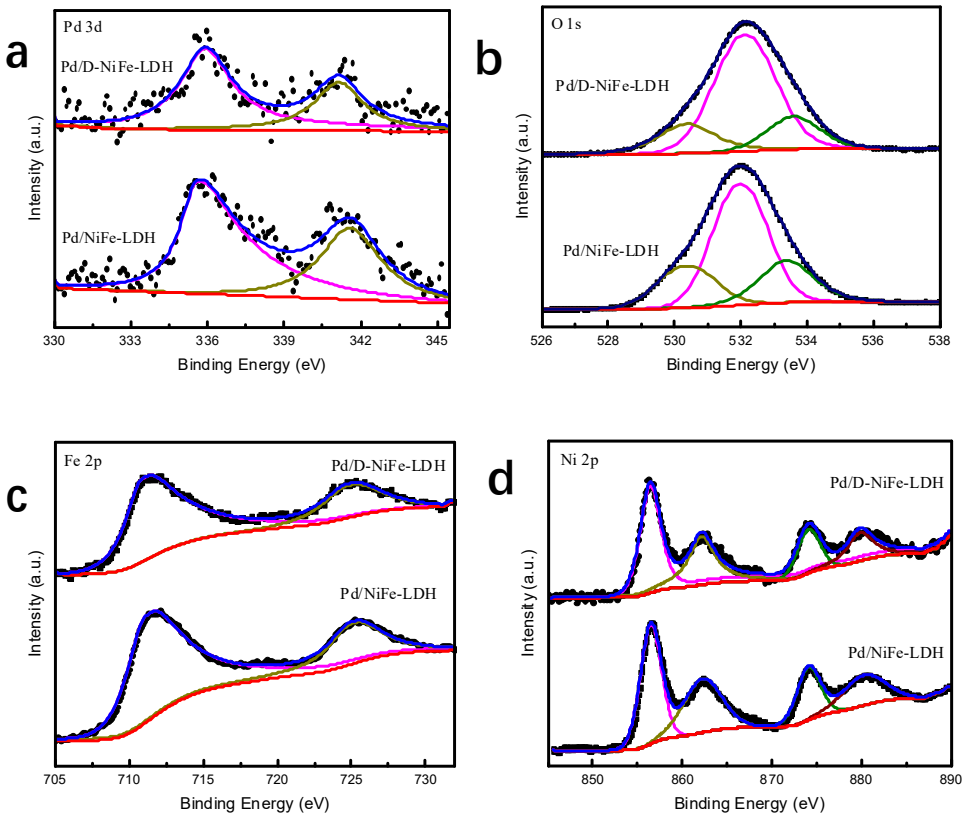

Figure S4. XPS spectra of Pd/D-NiFe-LDH: (a) Pd, (b) O, (c) Fe, and (d)Ni.

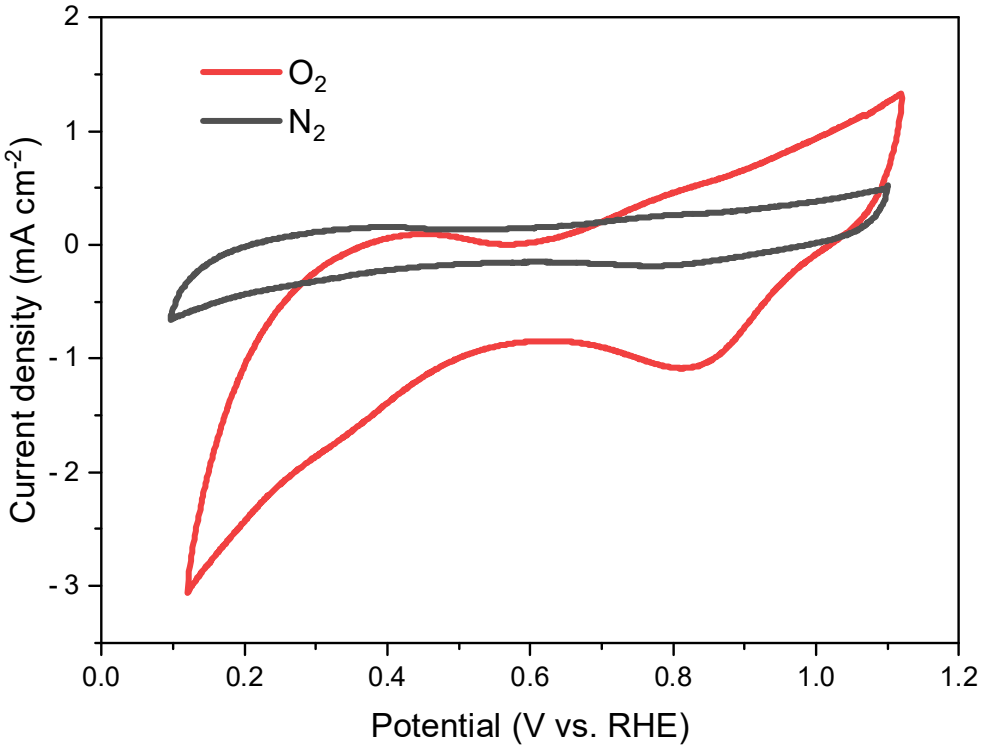

Figure S5. Cyclic voltammogram (CV) curves of Pd/D-NiFe-LDH in O_2 and N_2 (sweeping rate = 50 mV s-1).

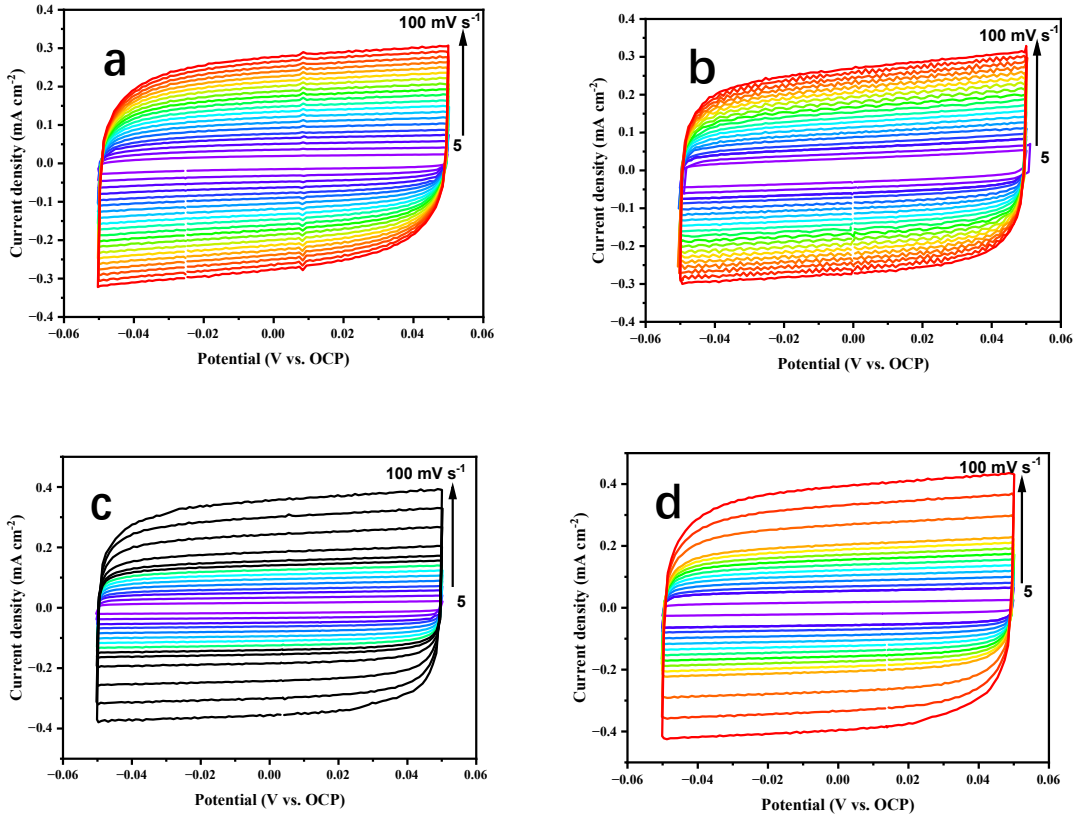

Figure S6. Cyclic voltammograms obtained at scanning rates from 5 to 100 mV-s^{-1}: (a) NiFe-LDH, (b) Pd/NiFe-LDH, (c) D-NiFe-LDH, and (D) Pd/D-NiFe-LDH.

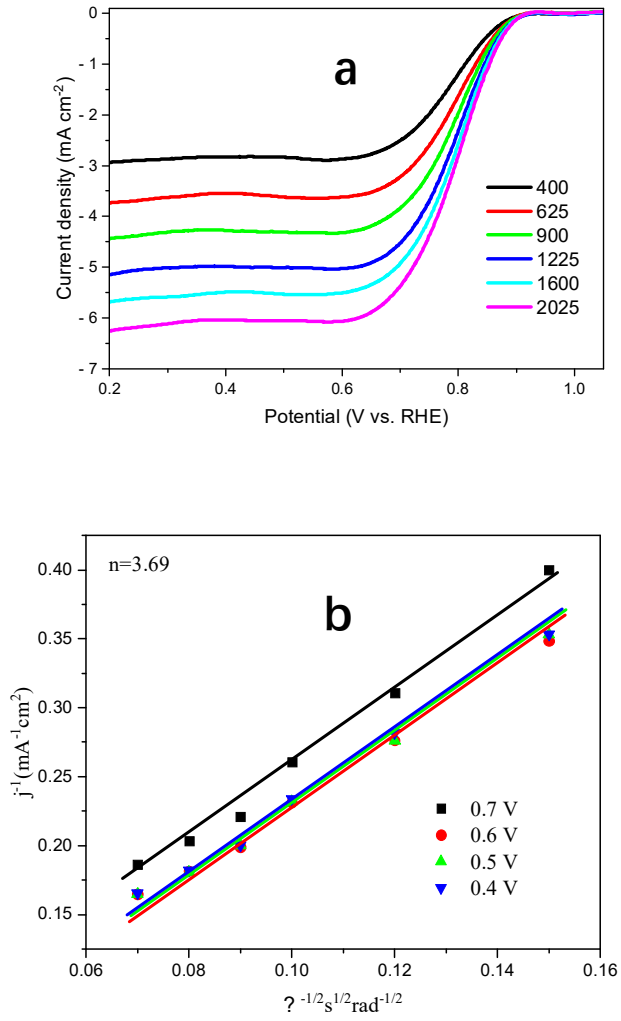

Figure S7. (a) LSV curves of Pd/NiFe-LDH at various rotation rates (scanning rate = 10 mV s^{-1}) and (f) Koutecky-Levich plots.

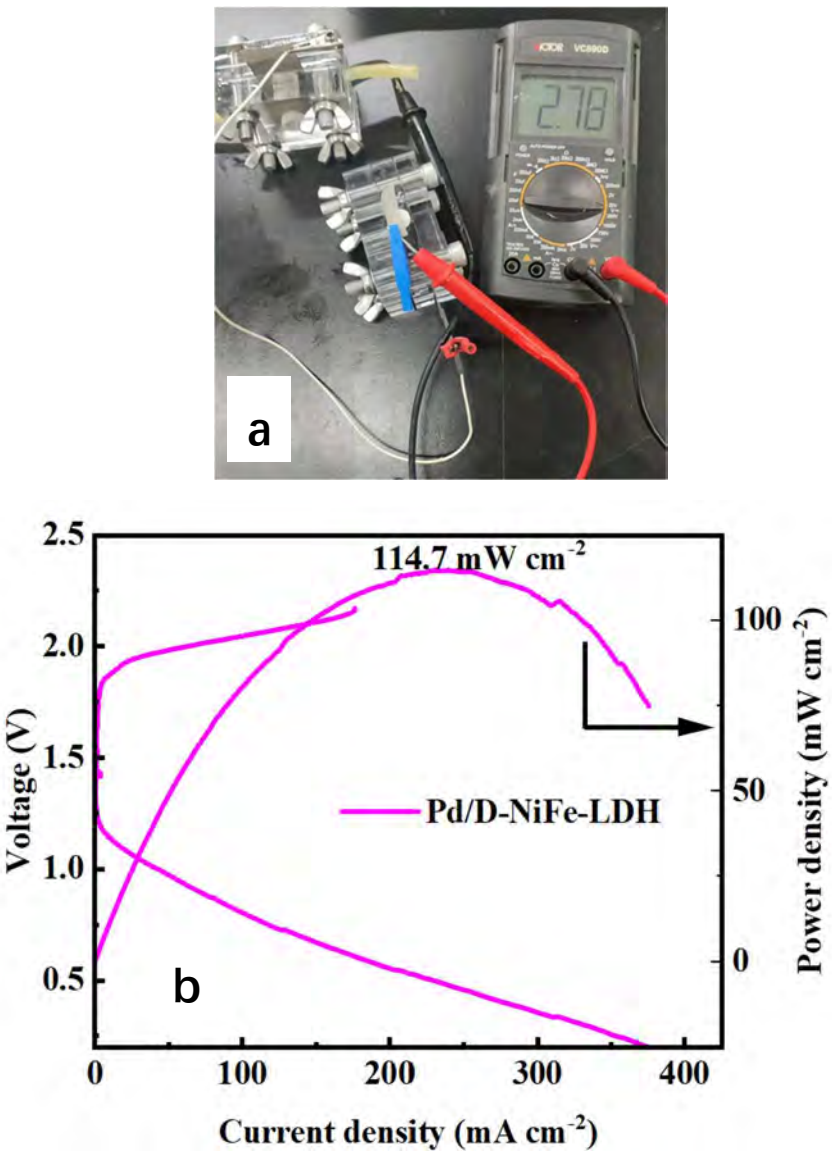

Figure S8. Homemade Zn-air battery with the Pd/D-NiFe-LDH cathode: (a) Open-circuit voltage and (b) Voltage during 1 hour, and (c) Full discharge profile at a current density of 1 mA cm^{-2}.

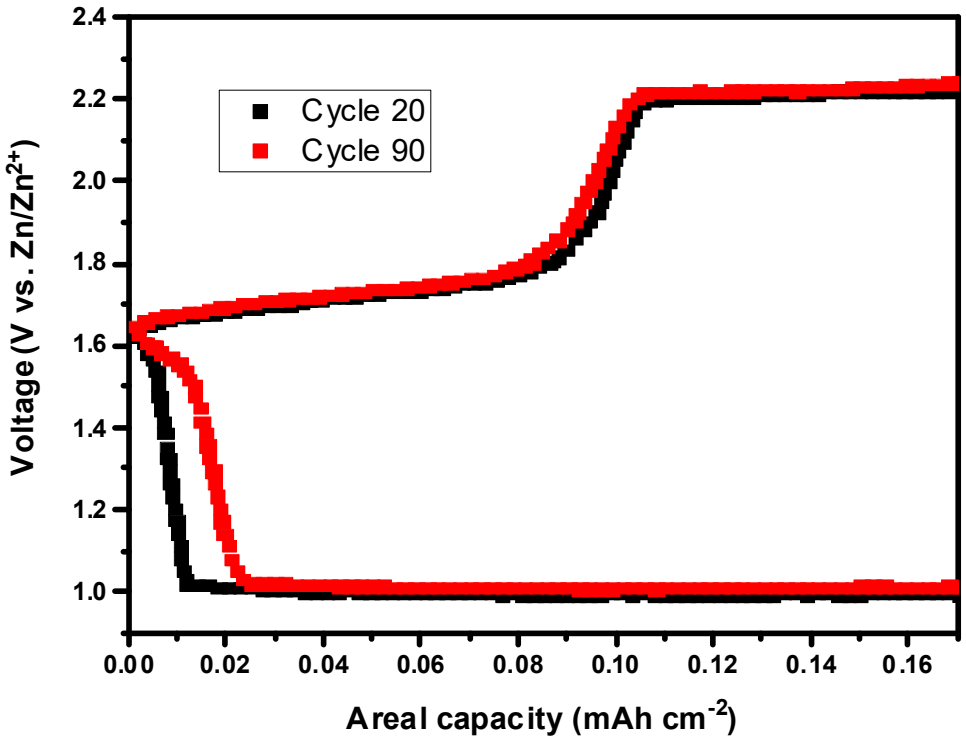

Figure S9. Galvanostatic voltage profiles of Zn-air battery composed of NiFe-LDH cathode at a current density of 2 mA cm^{-2}.

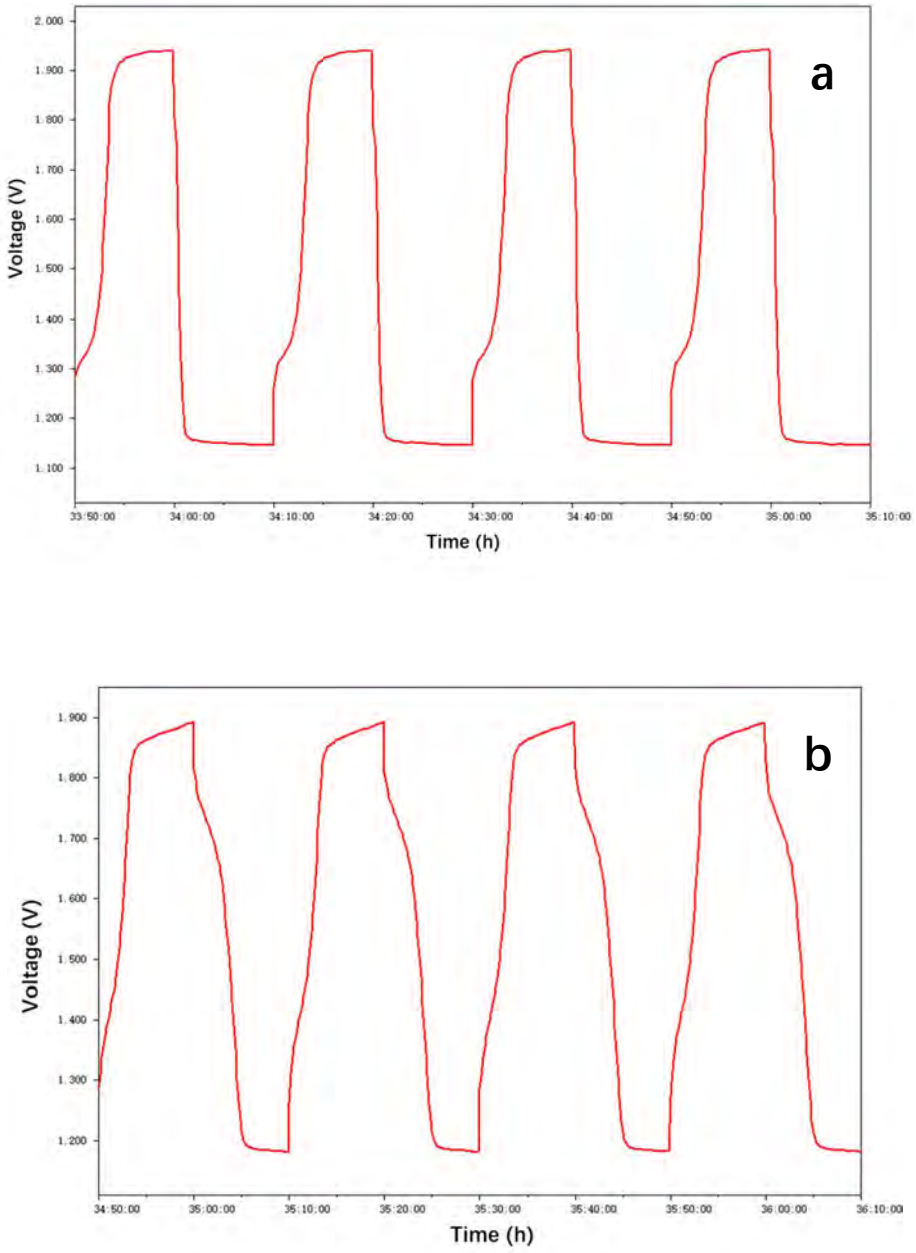

Figure S10. Charging/discharging curves (100 - 103th cycle) of the homemade Zn-air battery at a current density of 1 mA cm^{-2} with (a) Pd/NiFe-LDH and (b) Pd/D-NiFe-LDH cathode.

Table S1. Cyclability of Zn-air batteries.

Catalyst	Cyclability	Reference
Pd/D-NiFe-LDH	450 h at 2 mA cm^{-2}	This work
Ni-CAT/NiFe-LDH/CNFs	66 h at 1 mA cm^{-2}	[1]
$ZnCo_2Se_4$@rGO	114 h at 2 mA cm^{-2}	[2]
CFM-NC-800-RuO_2	80 h at 1 mA cm^{-2}	[3]
Fe_3Co_7-NC	400 h at 2 mA cm^{-2}	[4]
$Fe_{0.5}Co$@HOMNCP	120 h at 2 mA cm^{-2}	[5]
$NiCo_2O_4$-Cl^-HY	35 h at 2 mA cm^{-2}	[6]
Ce-Co_3O_4	280 h at 2 mA cm^{-2}	[7]
Co_2P/NP-CNTs-800	70 h at 2 mA cm^{-2}	[8]
CoZn@NC_IST	250 h at 2 mA cm^{-2}	[9]
Ni_3Fe-NCNTs-800	225 h at 2 mA cm^{-2}	[10]

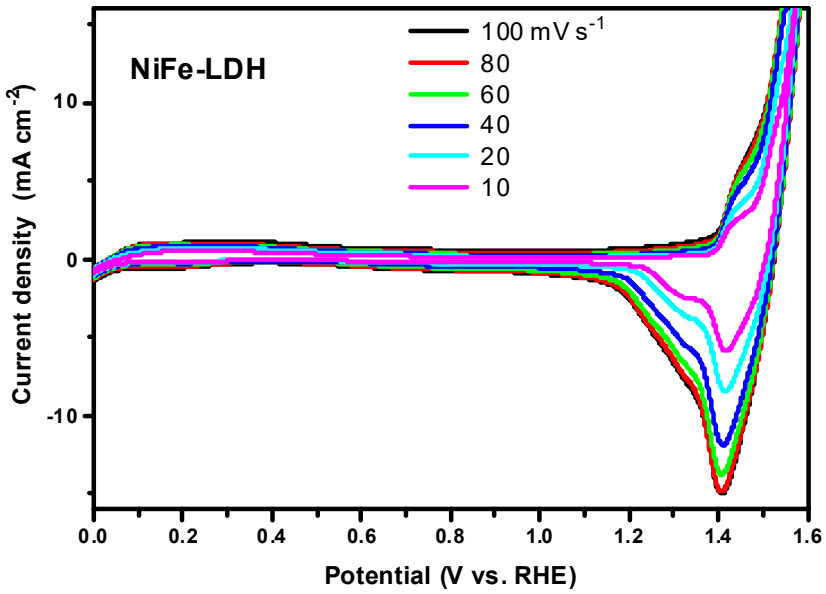

Figure S11. Cyclic voltammogram (CV) curves of NiFe-LDH in 1 mol L^{-1} KOH at different scanning rates.

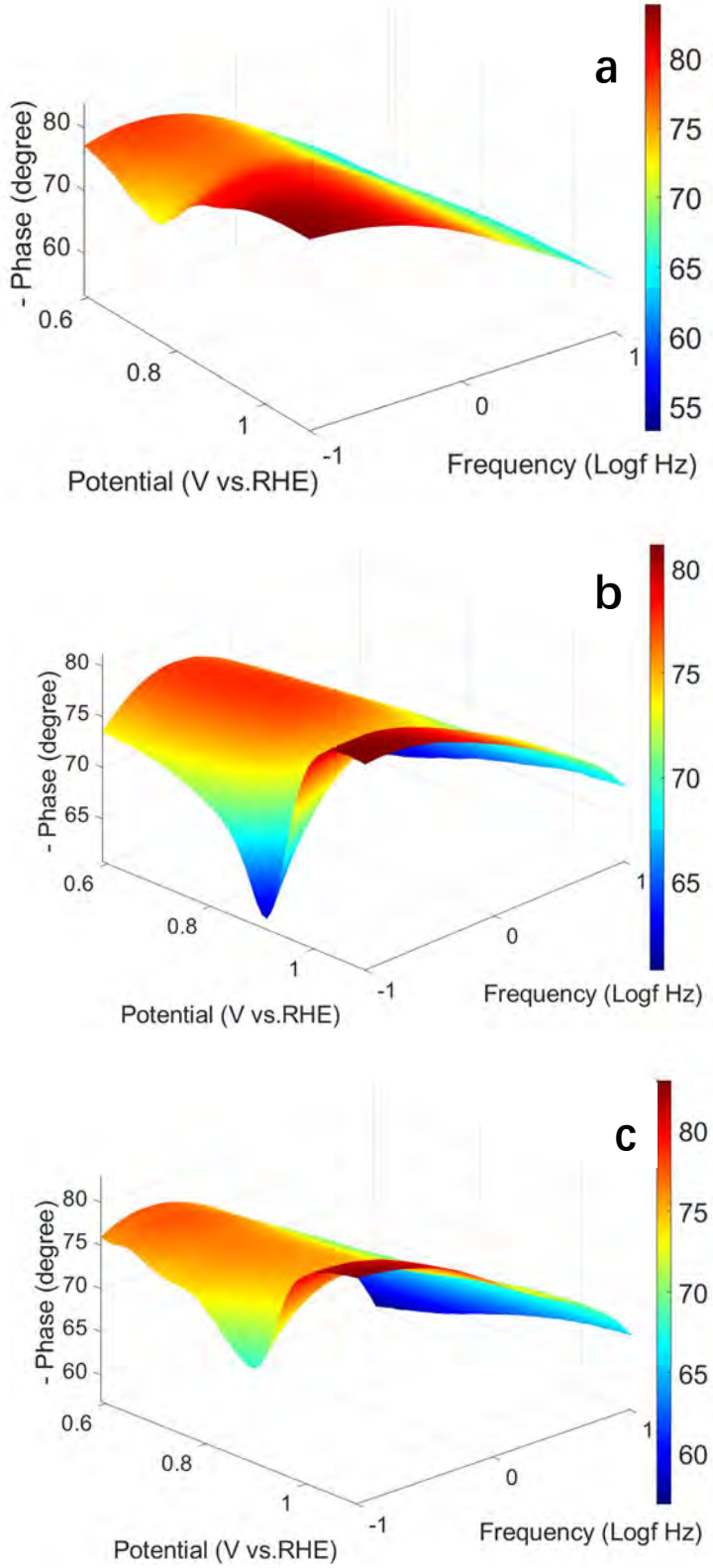

Figure S12. 3D pictures showing the phase angle versus frequency in the ORR potential region: (a) NiFe-LDH, (b) Pd/NiFe-LDH, and (c) Pd/D-NiFe-LDH.

References

[1] Li, J.; Qin, Y.; Bai, Z.; Li, S.; Li, L.; Ouyang. B.; Kan, E.; Zhang, W. Investigating the role of 3D hierarchical Ni-CAT/NiFe-LDH/CNFs in enhancing the oxygen evolution reaction and Zn-air battery performance. *Applied Surface Science*, **2024**, 648, 159080.

[2] Kumar, R. S.; Prabhakaran, S.; Ramakrishnan, S.; Karthikeyan, S. C.; Kim, A. R.; Kim, D. H.; Yoo, D. J. Developing Outstanding Bifunctional Electrocatalysts for Rechargeable Zn-Air Batteries Using High-Purity Spinel-Type $ZnCo_2Se_4$ Nanoparticles. *Small*, **2023**, 19(20), 2207096.

[3] Duan, X.; Xia, M.; Hu, X.; Yang, L.; Zheng, H. Interfacing MnO and FeCo alloy inside N-doped carbon hierarchical porous nanospheres derived from metal-organic framework to boost high-performance oxygen reduction for Zn-air batteries. *Nanoscale*, **2022**, 14(44), 16516-16523.

[4] Gu, T.; Zhang, D.; Yang, Y.; Peng, C.; Xue, D.; Zhi, C.; Zhu, M.; Liu, J. Dual-Sites Coordination Engineering of Single Atom Catalysts for Full-Temperature Adaptive Flexible Ultralong-Life Solid-State Zn-Air Batteries. *Advanced Functional Materials*, **2022**, 33(8), 2212299.

[5] Li, W.; Liu, B.; Liu, D.; Guo, P.; Liu, J.; Wang, R.; Guo,Y.; Tu, X.; Pan,H.; Sun D. Alloying Co Species into Ordered and Interconnected Macroporous Carbon Polyhedra for Efficient Oxygen Reduction Reaction in Rechargeable Zinc-Air Batteries. *Advanced Materials*, **2022**, 34(17), 2109605.

[6] Hu, W.; Bai, Y.; Yao, S.; Liu, Q.; Xu, X.; Lv, T.; Noreus, D. Boosting the

performance of Zn-air cells by spinel catalysts with bimodal pore structure and gill filament configuration. *Journal of Alloys and Compounds*, **2023**, 936, 168185.

[7] Qian, J.; Liu, X.; Zhong, C.; Xu, G.; Li, H.; Zhou, W.; You, B.; Wang, F.; Gao, D.; Cao, D. Enhanced Stability and Narrowed D-Band Gap of Ce-Doped Co_3O_4 for Rechargeable Aqueous Zn-Air Battery. *Advanced Functional Materials*, **2022**, 33(9), 2212021.

[8] Sun, T.; Li, T.; Han, D.; Liu, L.; Wang, H. N, P-doped carbon nanotubes encapsulated with Co_2P nanoparticles as efficient bifunctional oxygen electrocatalysts for rechargeable Zn-air battery. *Journal of Electroanalytical Chemistry*, **2023**, 928, 117016.

[9] Wang, Z.; Hou, X.; Dekyvere, S.; Mousavi B.; Chaemchuen, S. Single-thermal synthesis of bimetallic Co/Zn@NC under solvent-free conditions as an efficient dual-functional oxygen electrocatalyst in Zn-air batteries. *Nanoscale*, **2022**, 14(44), 16683-16694.

[10] Yan, Q.; Duan, X.; Liu, Y.; Ge, F.; Zheng, H. A hybridization cage-confinement pyrolysis strategy for ultrasmall Ni_3Fe alloy coated with N-doped carbon nanotubes as bifunctional oxygen electrocatalysts for Zn-air batteries. *Journal of Materials Chemistry A*, **2023**, 11(3), 1430-1438.